This is a preprint, the final version is subject to change, of the American Mineralogist (MSA)
Cite as Authors (Year) Title. American Mineralogist, in press.
(DOI will not work until issue is live.) DOI: http://dx.doi.org/10.2138/am-2017-5992

Revision 1

Structural characterization of marine nano-quartz in chalk and flint from North Sea Tertiary chalk reservoirs for oil and gas

VICTOR A. DRITS[1], JØRGEN SKIBSTED[2], OLGA V. DORZHIEVA[1,3], ANTHONY E. FALLICK[4] and HOLGERLINDGREEN[5]

[1.] *Geological Institute, Russian Academy of Science, Pyzhevsky per D7, 119017, Moscow, Russia*

[2.] *Department of Chemistry and Interdisciplinary Nanoscience Center (iNANO), Aarhus University, DK-8000 Gustav Wieds Vej 14,Aarhus C, Denmark*

[3.] *Institute of Ore Geology, Petrography, Mineralogy and Geochemistry, Russian Academy of Science, Staromonetny per D35, 119017, Moscow, Russia*

[4.] *Scottish Universities Environmental Research Centre, Rankine Avenue, East Kilbride, GlasgowG75 0QF, Scotland*

[5.] *Geological Survey of Denmark and Greenland, Øster Voldgade 10, DK-1350, Copenhagen K, Denmark*

Abstract

A new type of quartz, a nano-quartz consisting of spherical particles, is assumed to have formed by crystallization in the sea during sedimentation of the chalk in the North Sea and to have remained largely intact during burial diagenesis. The presence and nature of this nano-quartz have not been identified until recently, despite the fact that this quartz is the type present in the Upper Cretaceous-Danian chalk reservoir for oil and gas in the North Sea, both in the flint and as dispersed particles. In the present work detailed structural analysis of the nano-quartz has been carried out by X-ray diffraction, solid-state ^{29}Si and ^{27}Al MAS NMR, thermal analysis including water release, IR-absorption spectroscopy, and elemental analysis supplemented with analysis of oxygen isotope composition. It is found that ^{IV}Al substitutes for Si and that ^{VI}Al probably is bonded to hydroxyls on the particle surface of the nano-quartz structures. The charge compensation of tetrahedral Al^{3+}, in addition to its conventional way of compensation by formation of the local structural arrangement $[AlO_4/M^+]^o$ defects ($M^+ = H^+$, Na, K, Li), can occur at the expense of the OH^- group coordinating one of the four tetrahedral Si^{4+} nearest to the Al^{3+} tetrahedron. The most significant feature of the North Sea nano-quartz deduced in the present investigation is the presence of $[4H]_{Si}$ defects, also known as hydrogarnet defects. This defect is present in up to 5% of the tetrahedral sites, whereas Al^{3+} occupies less than 1% of the tetrahedral sites. Two types of distribution of the $[4H]_{Si}$ defects were determined. In one of them the $[4H]_{Si}$ defects aggregates parallel to the (0001) plane to form platelets as cracks with hydroxylated surfaces on both sides. The second type of $[4H]_{Si}$ defect occurs in the form of isolated tetrahedral vacant sites.The formation of the aggregated $[4H]_{Si}$ platelets lying in the (0001) plane mostly increases the *c* parameters of the structure whereas the isolated $[4H]_{Si}$defects and K+Na impurities contribute to increasing the *a* parameters.

The remarkable correlation of the positional distribution of the samples revealed from the relationships between *a*– and *c*–parameters and between amount of OH^- groups responsible for

formation of $[4H]_{Si}$ defects and *a*- and *c*-parameters can be considered as evidence for the validity of the structural formulae and, in general, of the main structural features of the studied samples. The unusually high content of $[4H]_{Si}$ defects in the nano-quartz samples may be related to their formation by precipitation in waters of the Danish North Sea.

Key words: Nano-quartz structure, nano-quartz formation, hydrogarnet defects, X-ray diffraction, ^{27}Al and ^{29}Si MAS NMR, IR spectroscopy, thermal water release, $\delta^{18}O$ isotope chemistry, elemental analysis.

Introduction

Quartz is the most abundant mineral on the Earth's surface and it is composed of nearly pure SiO_2that gives a strong X-ray diffraction (XRD) powder pattern with sharp *hkl* reflections. Quartz is usually crystallized during magmatism, metamorphism, hydrothermal reactions or during diagenesis at moderate to high temperatures. Despite the fact that sea water may be supersaturated with respect to quartz crystallization (Millot 1970), this type of crystallization is usually assumed to be too slow at ambient temperature to take place at a significant degree. However, an experimental study has demonstrated that quartz may form at Earth-surface conditions in sea water (Mackenzie and Gees 1971). Quartz is present as an accessory mineral in most carbonate rocks, often together with other silica minerals such as opal-CT and opal A. Usually quartz is assumed to have the well-established standard α-quartz structure, i.e., trigonal crystal system with space group $P3_221$ or $P3_121$. We have in detail investigated silica minerals from Danian chalk in six oil wells in the Danish part of the Central Graben in the North Sea, where the only silica mineral present is a new form of quartz composed of nano-size α-quartz spheres. The nano-quartz spheres are dispersed in the chalk matrix,

however, the flint in bands and nodules contains the same nano-quartz spheres (Jakobsen et al. 2000; Lindgreen et al. 2010, 2011). In some wells, the dispersed nano-quartz may constitute up to 70% of the chalk (Lindgreen et al. 2010).Quartz-rich layers are generally of low permeability and may act as internal seals for oil in chalk reservoirs (Lindgreen et al. 2010). Current theories assume that flint has formed through synsedimentary and post-depositional dissolution of Si-containing organisms in the chalk followed by migration and precipitation in hollows formed by dissolution of the chalk (Holmes 1965, p. 133-4; Bromley and Ekdale 1986; Clayton 1986; Zijlstra 1987; Madsen and Stemmerik 2010). However, the identical structure of the nano-quartz dispersed in the chalk and of the nano-quartz in the flint has, together with observations of structures in the sediments, formed the basis of a new model for formation of flint in North Sea chalk (Lindgreen et al. 2011): the nano-quartz in the flint, like the nano-quartz in the chalk matrix, has crystallized as nano-size particles in the marine Chalk Sea environment. The colloidal quartz particles have then flocculated and have been deposited on the sea floor mixed with calcitic bioclastic material. The pure flint probably formed during periods when decreased pH in the water column dissolved the calcite coccoliths during sedimentation and the silica was probably remolded after sedimentation (Lindgreen et al. 2011).

The unit cell parameters, as determined by X-ray diffraction, for natural quartz may show a variation of up to 0.03%, and there is a trend of increasing cell size with decreasing metamorphic grade (Hurst and Storch 1981).In the North Sea nano-quartz, the unit-cell parameters, sizes of coherent scattering domains (CSDs) and strain values deviate from those of normal α-quartz, the *a* and *c* cell parameters being larger by as much as 0.10% (Lindgreen et al. 2011). Substitution, such as Al^{3+} for Si^{4+}, has been deduced for quartz (Dennen 1966; Dennen and Blackburn 1970), however, the substitution was deduced from elemental analysis and cell parameters. Application of high-resolution Electron Paramagnetic Resonance (EPR) spectroscopy to the study of paramagnetic

93 defects in a large collection of crystalline quartz samples has shown following centres originating
94 mostly from impurity ions: H, Al, Cu, Ag, Ge, P, Ti, and Fe (Weil 1984). According to the EPR
95 data all Al-associated paramagnetic centres in quartz have shown that Al^{3+} occurs exclusively at the
96 tetrahedral sites (Weil 1984, 2000; Botis and Pan 2009). Using ab initio calculations at the density
97 functional theory level, Botis and Pan (2009) investigated the nature of the $[AlO_4/M^+]^o$ defects
98 (M^+= H, Li, Na, and K) and showed them to be stable in the α-quartz structure. The $[4H]_{Si}$ defect,
99 the so-called hydrogarnet defect, where vacant tetrahedral sites have 4 adjacent OH^- groups, is a
100 common defect in quartz, especially synthetic quartz (McLaren et al. 1983; Shinoda and Aikawa
101 1993; Cordier et al. 1994; Lin et al. 1994; McConnell et al. 1995; McConnell 1996; Rosa et al.
102 2005; Stalder and Neuser 2013).The $[4H]_{Si}$ defect can cause development of planar defects in quartz
103 in the vacuum and temperature of the electron microscope (McConnell et al. 1995). Rosa et al.
104 (2005) calculated that the $(OH)_4$ group is the thermodynamically most stable water-related defect
105 and suggested that the $(OH)_4$ defects are likely to form platelets lying in the (0001) plane.The
106 objective of the present investigation is a detailed analysis of the nano-quartz by X-ray diffraction,
107 solid-state MAS NMR, IR-absorption spectroscopy, thermal analysis including analysis of water
108 release, and elemental analysis by atomic absorption spectrometry (AAS) in order to reveal the
109 particular structural and crystal-chemical features of flint and dispersed particles of nano-quartz.
110
111 **Materials**
112
113 The chalk matrix and flint from the Tertiary Danian chalk in Danish North Sea were
114 investigated. Cores from the wellsSif-1 and Nana-1 in the Halfdan Field, from well E-5 in the Tyra
115 Field and from well M-10 in the Dan Field have been sampled. Samples taken from two cores in
116 Sif-1, comprising both flint and chalk, are shown in Figure 1.

The flint samples were crushed to <0.25 mm in a mortar before investigation, whereas the chalk samples were crushed to <2 μm before removal of calcite. Preliminary study of the samples allowed a choice of only impurity free samples for the future investigations. One flint sample 5 (Sif-1, 2057.63) (Table 1) was heated to 605°C for two hours and then investigated at room temperature by XRD and NMR to observe the structural effects of the heating.

Methods-experimental

Removal of calcite

The large amounts of calcite in chalk have been removed by dissolution prior to the mineralogical investigations of the non-calcite minerals. The chalk samples were crushed to pass a 4 mm sieve. The samples were then added to 200 ml of distilled water, and the calcium carbonate was removed by adding acetic acid while keeping the solution buffered at pH 4.5 to 5. The supernatant was removed by centrifugation and the residues were washed with distilled water to remove excess ions, and air-dried. This buffered dissolution of calcite was applied in order to avoid corrosion or dissolution of the fine-grained non-calcite minerals, such as the clay minerals and nano-quartz. Clay minerals and other mineral impurities were not detected by XRD and carbonates were not present according to DTA-EGA (the CO_2 evolution curve).

Atomic force microscopy

Atomic Force Microscopy (AFM) was carried out using a Rasterscope 3000 instrument. Intact rock specimens were small pieces of chalk or flint glued onto gold-coated sample holders. In samples with small amounts of non-calcite minerals these could only be identified and imaged in residues. For such samples, the residues were dispersed ultrasonically in distilled water and the

specimens prepared by leaving a drop of the suspension to dry under ambient conditions on a block of highly oriented pyrolytic graphite. AFM was carried out at ambient conditions with the tip running in non-contact mode, a force of 0.175 nN and a scanning speed of 500 nm/s.

X-ray diffraction

The flint samples were crushed by hand in a mortar to pass a 250 μm sieve whereas the residual samples were processed after removal of calcite. XRD patterns were obtained using Co*K*α radiation with a Philips PW3040 diffractometer having a vertical goniometer PW3050 with a curved graphite monochromator and a fine-focus tube. Randomly oriented specimens were analyzed using 1° fixed divergence and anti-scatter slits and intensities were measured for 40 s per 0.02 °2θ step in the range 23–91°2θ. An internal standard of 5% Si was used.

Determination of the unit cell parameters. This procedure included the following steps: (1) calibration of *hkl* peak positions using those of Si as an internal standard; (2) removal of the contribution of K_{α_2} from each *hkl* peak mathematically, assuming that profiles of both K_{α_1} and K_{α_2} maxima are described by the same Pearson function which provided a fit with R_{W_P}< (2-4) %; (3) the profile of each individual *hkl* peak corresponding to K_{α_1} was used to determine its position (2θ) and *d* value. The Jade® computer program was used for the determination of the unit cell parameters by the least-squares method.

Determination of the mean size of coherent scattering domains, CSD's, and microstrains. The effective breadth of each *hkl* reflection corresponding to$K_{\alpha_1}$is determined as a ratio of its area to amplitude. These values were determined for *hkl* reflections of a sample and for those of a flat

perfectly crystalline Si standard. To a fair approximation the breadth, B, of an experimental reflection is described by the equation (Moore and Reynolds 1997):

$$B^2 = \beta^2 + \beta_{st}^2 , \qquad (1)$$

Whereβ is the pure, undistorted breadth in degree 2θ (in radians) and β_{st} is the same quantity for a peak from the crystalline Si standard. A reflection breadth, β, is determined by the influence of two main parameters, having different dependences on θ. One of themβ_L is related to the mean size of coherent scattering domains, L, according to the Scherrer equation:

$$L = k\lambda/\beta_L \cos\theta , \qquad (2)$$

where θ and λ are the angular position of the studied *hkl* reflection and the wave length, respectively.

The second factor, β_{str}, is controlled by microstrains determined by a relative variation of d-spacing $|\Delta d/d|$ at each given θ and depends on θ as:

$$\beta_{str} = |\Delta d/d| \tan\theta. \qquad (3)$$

A mutual influence of both factors determines the breadth, β, of the experimental reflection which to a good approximation is related to β_L and β_{str} as:

$$\beta^2 = \beta_L^2 + \beta_{str}^2 . \qquad (4)$$

Thus, to determine both a mean size of CSD's and microstrains along a normal to the (*hkl*) plane requires the use of the βvalues for at least two reflections having two orders of *hkl* indices, for example 100 and200. Solution of two equations (4) for β_{100} and β_{200} allows calculation of the values of interest.

Solid-State NMR Spectroscopy

Solid-state ^{27}Al and ^{29}Si experiments were performed on Varian Direct-Drive VNMRS-600 (14.09 T) and Varian INOVA-400 (9.39 T) spectrometers, respectively. The ^{27}Al MAS NMR

spectra were acquired with a home-built CP/MAS probe for 4 mm o.d. zirconia (PSZ) rotors, using a pulse width of 0.5 μs and a rf field strength of $\gamma B_1/2\pi$ = 50 kHz (i.e. a flip angle < $\pi/6$ for ^{27}Al, I = 5/2, in a solid) to ensure quantitative reliability of the intensities, observed for the ^{27}Al central transition for sites experiencing different quadrupole couplings. Moreover, ^{1}H decoupling ($\gamma B_2/2\pi$ = 50 kHz), a spinning speed of ν_R = 13.0 kHz, and a relaxation delay of 2 – 4 s were employed. The ^{27}Al MAS spectrum of the probe itself with an empty spinning (ν_R = 13.0 kHz) PSZ rotor showed a broad resonance of very low intensity. This spectrum was subtracted from the ^{27}Al MAS spectra of the quartz samples prior to the quantitative evaluation of the observed intensities. The ^{29}Si MAS and ^{29}Si{^{1}H}CP/MAS NMR experiments (9.39 T) used a home-built CP/MAS probe for 7mm o.d. rotors and spinning speeds of ν_R = 6000Hz and ν_R = 4000Hz, respectively, and rf field strengths of $\gamma B_1/2\pi = \gamma B_2/2\pi$ =49 kHz for ^{29}Si and ^{1}H. The single-pulse experiments employed a 45^{o} excitation pulse whereas the CP/MAS experiments used a standard CP rf-pulse sequence with ^{1}H TPPM decoupling during acquisition. ^{29}Si chemical shifts are referenced to an external sample of tetramethylsilane (TMS), while ^{27}Al chemical shifts are referenced to an external sample of a 1.0 M aqueous solution of $AlCl_3 \cdot 6H_2O$.

Elemental composition by Atomic Absorption Spectrometry (AAS)

EDAX analysis of dispersed nano-quartz showed that Si is dominant and only minor amounts of Al, Na and K are present in the nano-quartz. Other major elements were not detected in significant amounts except for traces of Ca in the residues because Ca in these samples was present as adsorbed cations residual from the removal of calcite. Because of the small contents of cations other than Si, total chemical analyses were made using HF-H_3BO_3 dissolution in Teflon vessels (Bernas 1968) followed by AAS determination of dissolved Al, Na and K. The AAS determination, using a Perkin Elmer Analyst 400 spectrometer, is more accurate than the XRF method especially

for the light elements, Na and Al, and in general when the content of cations is low. The amounts of Al_2O_3, K_2O and Na_2O were determined by AAS using nitrous oxide-acetylene flame for Al and air-acetylene flame for Na and K. The absorption standard curve was linear in the ranges 0.5-1.0 ppm found in the solutions for the three elements. The dissolution method of Bernas (1968) results in solutions having a very low ionic strength which is very important for accurate AAS determinations at low concentrations, the matrix effect being minimal. The possible errors in estimation of the weight amounts of Al_2O_3, Na_2O, and K_2O varied from 5 to 15%. The large amounts of Si did not allow an accurate determination of Si better than ±1%. The flint samples were raw samples and probably had Na^+ from pore water adsorbed, whereas the chalk residue samples were Ca^{2+}-saturated, because the buffered dissolution of the calcite left the solution with Ca^{2+} as the dominant cation. Al was divided into ^{IV}Al and ^{VI}Al based on the ^{27}Al NMR analyses.

Infrared spectroscopy

Mid-infrared absorption spectra were obtained at room temperature in transmission mode using a Bruker Vertex 80v FTIR spectrometer, coupled with a Hyperion 1000 microscope using a liquid nitrogen cooled MCT detector and a KBr beamsplitter. 600 scans in a range of 3700-3200 cm^{-1} were recorded with a spectral resolution of 2 cm^{-1}. Flint specimens were prepared as both side polished plates with 50 μm thickness whereas residual specimens were recorded from thin layers of powder where the thickness was not controlled.

Each spectrum was analyzed using the OPUS 7.1 software. Baseline correction was performed automatically by the "Concave Rubberband" OPUS function (number of iterations – 15, number of baseline points – 64). Smoothing was also carried out automatically (number of smoothing points – 13). The position of bands was determined by the second derivative and decomposition of the partially overlapping bands. For each studied sample 4-6 spectra were

obtained from different parts of the specimen because samples had a certain degree of heterogeneity of density.

Thermal analysis (DTA-EGA)

Thermal analysis was carried out using a Stanton-Redcroft DTA 673-674 instrument with gas outlet to non-dispersive infrared H_2O and CO_2 detectors (Morgan 1977). The sensitivity using infrared detection is very high and makes it possible to quantify carbonates and water release separately (Morgan 1977). The gas (in the present case analytical grade N_2) flowed through an oven with a specially designed outlet at the top and then through first the IR detector for H_2O and then the IR detector for CO_2. Both detectors were measuring the gases at a 1000 ppm scale. Furthermore, flow controllers stabilized the flow at 400ml/min. A run with $CuSO_4 \cdot 5\ H_2O$ was used for calibrating the H_2O release. A flow of analytical grade N_2 was used before each sample run until the baselines for the gases were horizontal, the heating was then initiated at 10°C/min until 1000°C. Peak areas were determined by integration. The overall accuracy of the determinations was about 10% relative. Both H_2O and CO_2 were determined, which is an advantage compared to thermogravimetric analysis where overlap may occur. The analyses showed that carbonates were not present in the flint samples or in the residue samples after dissolution treatment.

Isotope geochemistry

$\delta^{18}O$ of silica samples was determined by the Macaulay et al. (2000) modification of the laser fluorination procedure of Sharp (1990). The precision and accuracy of the measurement of the oxygen isotopic composition of the CO_2 are ± 0.2‰ (1σ) and NBS 28 gives 9.6‰; data are reported as δ values in ‰ relative to V-SMOW. The samples were vacuum degassed overnight at room

259 temperature to remove labile adsorbed species; higher temperature was not employed to avoid
260 possible loss of structural water and hydroxyl, which may have differentially affected the samples.
261
262 **Results**
263
264 **Atomic force microscopy**
265 Atomic force microscope images of the two studied samples – a residue from chalk sample 12
266 (Sif-1, 2071.13) and from a flint sample 13 (Sif-1, 2079.34) are shown in Figures 2a and b. Note the
267 similarity in structure: both are composed of nano-size spherical or rounded particles. These
268 features are seen especially well in Figure 2a.
269
270 **X-ray diffraction**
271 19 samples were studied using the X-ray diffraction, the list of which is given in Table 1. X-
272 ray diffraction for the region 20–90°2θ for a residue sample 12 (Sif-1, 2071.13 m), a flint sample 13
273 (Sif-1, 2079.34 m) and the standard quartz are shown in Figure 3a, b, and c, respectively. The peak
274 height is considerably larger for the standard quartz compared to the two nano-quartz samples,
275 when the standard Si added is used as a reference. The largest discrepancy between the two nano-
276 quartz samples and the standard quartz is observed in the high-angle region 80–82°2θ, where the
277 sharp 212, 203 and 301 peaks of the standard quartz are strongly different from the broad and
278 poorly resolved peaks of the two nano-quartz samples (Figure 3d). However, the high-angle
279 patterns for the residue nano-quartz and for the flint nano-quartz are very similar. The observed
280 significant broadening of the reflections results from microstrains having high values (Table 1).
281 The quartz from the chalk and flint samples has a three-dimensional periodicity of the lattices
282 and is characterized by having significantly larger *a*– and *c*–parameters as compared to those of

normal quartz (Table 1). The range of the parameter variation is from 4.9164 Å to 4.9195 Å for the *a*–parameter, and from 5.4047Å to 5.4097Å for the *c*–parameter, whereas the standard Merck quartz has an *a*–parameter of 4.9144Å and a *c*–parameter of 5.4055 Å (Table 1). Another distinguishing feature is that the quartz in the studied samples consists of much smaller CSD's compared to those of normal quartz (Table 1). The values of L_{100} of the studied quartz vary from 56 to 72 nm for the chalk and from 47 to 70 nm for the flint samples (Table 1). The L_{101} values of the quartz also vary within similar intervals: 67–84 nm for the chalk and 56–88nm for the flint samples (Table 1). Note that microstrains have similar values along both studied crystallographic directions (Table 1).

The XRD pattern of the sample 5 (Sif-1, 2057.63), which had been heated to 605°C for two hours, was identical to the pattern of the natural sample.

MAS NMR

14 samples were studied using the ^{27}Al MAS NMR, the list of which is given in Table 2. The ^{27}Al MAS NMR spectra of three nano-quartz samples are shown in Figure 4. The spectra of samples 7 (Sif-1, 2065.0, flint), 10 (Sif-1, 2071.08, chalk) and 17 (Nana-1, 2135.8, flint) are dominated by a resonance with a center of gravity at 56 ppm, originating from Al in tetrahedral coordination. The peak falls in the chemical shift range for framework $Al(–O–Si)_4$ sites and thus it is assigned to Al^{3+} substituting for Si^{4+} in the tetrahedral sites of the quartz structure, following an earlier ^{27}Al NMR study of the incorporation of Al^{3+} guest ions in calcium silicate phases (Skibsted et al. 1994). A minor peak at 4 – 5 ppm is also observed for all samples whereas the ^{27}Al MAS NMR spectrum of the flint sample 7 (Sif-1, 2065.0) in addition includes a small resonance at 14 ppm. The 4–5 ppm peak has almost the same chemical shift and line shape as observed for octahedral aluminate species in ^{27}Al MAS NMR spectra of calcium-silicate-hydrate (C-S-H) phases

307 resulting from Portland cement hydration (Andersen et al. 2006) and for dioctahedral Al-rich
308 2:1clay minerals (Sanz and Serratosa 1984; Sanz 1990; Takahashi et al. 2008). In the work of
309 Andersen et al. (2006) the origin of the octahedral Al resonance at 5 ppm was investigated in detail
310 for several different samples, using different NMR techniques, and it was finally assigned to
311 nanostructured aluminate species, including $Al(OH)_6^{3-}$ or $O_xAl(OH)_{6-x}^{-3-x}$ sites, formed on the
312 surface of the C-S-H phase. Following this assignment, and the strong similarity in ^{27}Al chemical
313 shift and linewidth, the observed ^{VI}Al resonance at 4 – 5 ppm (Figure 4) will be ascribed to
314 octahedral $Al(OH)_3$ sites formed at the surface of the quartz crystals. The ^{27}Al MAS NMR spectra
315 allow determination of the relative fractions of aluminum atoms in the different coordination
316 environments as summarized for the samples in Table 2.
317 The ^{29}Si MAS NMR spectra of the four studied samples – two flint samples 7 (Sif-1, 2065.0)
318 and 17 (Nana-1, 2135.8), the chalk quartz sample 10 (Sif-1, 2071.08), and the commercial quartz
319 (Figure 5) all contain a narrow resonance at –107.4 ± 0.2 ppm, in accordance with the well-known
320 chemical shift for α-quartz (Lippmaa et al. 1980, Spearing and Stebbins 1989) with its crystal
321 structure containing fully condensed SiO_4 tetrahedra (i.e. Q^4(4Si) sites). The line width of the
322 resonance varies around FWHM = 0.60 ppm (sample 10, Sif-1, 2071.08, chalk) for the studied
323 nano-quartz samples whereas it is significantly smaller for the commercial quartz (FWHM = 0.22
324 ppm). Impurity ions in the quartz lattice may distort the nearest SiO_4 tetrahedra and thereby result in
325 an increased linewidth. Moreover, Si sites near the surface of the crystallites will exhibit some
326 distortion/tension which will contribute to the line width as well. Thus, the significantly smaller line
327 width for the commercial quartz reflects that the crystallites in this sample are much larger than
328 those of the core samples, combined with a smaller fraction of impurity ions in the commercial
329 quartz sample. The crystallites of the nano-quartz samples are rather similar in size, and therefore
330 the variations in line width primarily reflect variations in impurity ions in the crystal lattices. These

results are in agreement with small sizes of CSD's and high values of microstrains which provided a significant broadening of *hkl* reflections in the XRD pattern of the studied samples.

Improved information about the surfaces in the nano-quartz samples is obtained from $^{29}Si\{^{1}H\}$ CP/MAS NMR spectra (Figure 6) acquired using three different CP contact times (τ_{CP} = 2.0, 4.0, and 8.0 ms). These spectra only include resonances from Si sites with hydroxyl groups or bound water molecules in the near vicinity. The resonance at –107.4 ppm is observed for all nano-quartz samples and with increasing intensity on going from a contact time of 2.0 ms to 8.0 ms. The observation of this resonance may reflect that the surface is hydrated or hydroxylated since the resonance originates from Q^4(4Si) sites with structural environments in which Si cations interact directly with hydroxyls or water molecules. Therefore, this resonance most likely originates from hydroxylated surfaces formed by aggregation of empty tetrahedral sites that have four adjacent OH^- groups bonded to Si in adjacent tetrahedral sites, the $[4H]_{Si}$ hydrogarnet defect (Figure 7) (McLaren et al. 1983; Shinoda and Aikawa 1993; Cordier et al. 1994; Lin et al. 1994; McConnell 1996; de Leeuw et al. 1999; Rosa et al. 2005). The $^{29}Si\{^{1}H\}$ CP/MAS NMR spectra of the nano-quartz samples also include a peak at higher frequency which seems to originate from two overlapping resonances, corresponding to a high-frequency shoulder at –97.6 to –98.0 ppm and the most intense component in the range –99.6 to –99.8 ppm for the three nano-quartz samples. Following earlier studies of silica gels and highly siliceous zeolitic framework structures, these resonances reflect the hydroxylated surface and empty tetrahedral sites with OH^- bonded to Si^{4+}. Therefore, the resonances at –99.6 to –99.8 and at –97.6 to –98.0 ppm can be assigned to the overlapping peaks from $(Si–O)_3–Si^*–OH$ sites which contain the $[4H]_{Si}$ hydrogarnet defects distributed in the form of aggregates (Figure 7) and isolated defects (Figure 8a), respectively. The $^{29}Si\{^{1}H\}$ CP/MAS NMR spectra of the studied samples contain also two overlapping peaks located at –94.0 ppm and–91.7 ppm both having very low intensity. The highest intensity for the overlapping –91.7 and –94.0 ppm

resonances is observed for the shortest contact time (τ_{CP} = 2.0 ms), indicating that they originate from Si sites in the very near vicinity of H atoms. Following the information derived from the ^{27}Al MAS NMR spectra of the samples (vide infra), these peaks are ascribed to surface sites of the type $(Si–O)_2–Si^*–(OH)_2$and $(Si–O)_2–Si^*–OH–OAl$, where the latter represents a Q^3(Al)site where Si is next nearest neighbor to a hydroxylated Al^{3+} having tetrahedral coordination. The presence of such Al–H defect sites in the studied samples is determined by IR (see below).

Infrared spectroscopy

11 samples (# 2, 3, 5, 7, 8, 9, 12, 14, 17, 18, and 10) were studied by infrared spectroscopy. The characteristic feature of the IR spectra of the studied nano-quartz samples that strongly distinguish them from spectra of natural quartz of different origins is the presence of two most intense and closely located OH absorption bands at 3588 and 3613cm^{-1} (Figure 9). Individual positions and intensities of these partially overlapping bands were determined by second derivatives with a subsequent decomposition procedure (Figure 9). The ratio of intensities for these bands at 3588 and 3613 cm^{-1} corresponding to the spectra having different integrated intensities of the partially overlapping bands is close to 2:1 (Figure 10) showing that the origins of these bands are somehow interrelated. Other diagnostic regions of the IR spectra may also be divided into two groups. One of them contains two wide and weak OH absorption bands at 3378–3381cm^{-1}and 3436–3444cm^{-1}whereas the second group in addition contains the third band at 3473 – 3474cm^{-1} (Figure 9). Unfortunately, it was not possible to obtain a homogeneous and uniform thickness of the specimens of the different samples for the acquisition of the IR spectra. Moreover, intensities of the absorption bands were varied in the IR spectra obtained from different specimens of the same sample. For example, in different spectra of sample 14 (Sif-1, 2088.3) the maximal and minimal intensities of the bands at 3588cm^{-1} differ from each other by almost five times. However, after

normalization of these spectra to that having the highest intensity of the bands at 3588 and 3613 cm^{-1}, intensities and profiles of the other bands having lower frequencies are almost identical or very similar. It was concluded that the main factor responsible for the observed intensities variation in the spectra from different parts of the same sample is related to different thicknesses of these parts. Therefore, intensities of the bands in each spectrum were normalized to that of the band at 3588 cm^{-1} which was the same in all spectra and equal to 100% in arbitrary units.

Thermal analysis (DTA-EGA)

14 samples were studied using the thermal analysis, the list of which is given in Table 3 and 4. The curves for evolved water (EWA) for all samples have a peak at ~570°C (Figure 11) and some have an additional peak at ~360°C (Table 3).Two flint samples, 8 (Sif-1, 2066.3) and 9 (Sif-1, 2070.94), have practically identical EWA curves. The H_2O evolution curve for the residue sample 12 (Sif-1, 2071.13) has a double peak at 570°C and 650°C (Figure 11). The amount of water released above 300°C during heating varies from 0.30% to 2.1% (Table 3). Usually, DTA curves for quartz have an exothermic peak at 573°C due to the $\alpha \rightarrow \beta$ transition at this temperature. This peak was not detected in the DTA curves of the nano-quartz samples, despite the fact that this peak usually is very sharp for quartz. This lack of a sharp peak at the $\alpha \rightarrow \beta$ transition temperature probably reflects that the first-order character of the transition is strongly reduced in natural nano-size quartz because of the clamping imposed on each grain by the surrounding nano-crystallites (Rias et al. 2001). In addition, one has to take into account that the hydrogarnet defect incorporation in quartz is an endothermic reaction (Rosa et al. 2005) and thus, the hydrogarnet dehydroxylation also should have the same nature. Surface-adsorbed H_2O is released at low temperature, up to 200°C. The release of the H_2O at ~550°C seen in EWA for the North Sea quartz (Figure 11, Table 3) corresponds to the release of OH^- from the $[4H]_{Si}$ defect at 550°C observed by McLaren et al.

(1983), but includes also the release of OH^- from $Al(OH)_3$ at the particle surfaces. OH^- groups at the surfaces of silica minerals are released continuously as the temperature increases (Segnit et al. 1965).

Structural formulae

The samples contain 0.11–0.73% Al_2O_3, 0.016–0.60% Na_2O and 0–0.22% K_2O (Table 2, these values were estimated with relative errors 5–15%). According to the ^{27}Al MAS NMR spectra, each sample contains tetrahedral and octahedral Al sites (Table 2). The results of thermal analysis showed that the weight content of H_2O released from the samples heated from 300 to 560-600°C varies from 0.30% to 2.10% with relative errors of 10% or lower (Table 3). According to the ^{27}Al MAS NMR data, each sample can be considered as a physical mixture of two phases: bulk nano-quartz incorporating tetrahedral Al sites and an $Al(OH)_3$ phase with octahedrally coordinated Al formed at the surface of nano-crystals of quartz. In the general form, the structural formula may be presented as:

$$Na_\alpha K_\beta (Si_{(1-\square y-\gamma)}{}^{IV}Al_\gamma)O_{2-x}OH_x$$

The total molar amount of Al was calculated using the ratio of corresponding weight amount of Al_2O_3 to its molar weight, whereas the amount of ^{IV}Al and ^{VI}Al were determined using the total molecular amount of Al and the $^{IV}Al/^{VI}Al$ molar ratio from the ^{27}Al MAS NMR spectrum of the sample. Na_α and K_β are molar amounts of Na and K in the sample, OH_x is equal to the difference between the total molar amount of OH groups in the sample and that related to the molar amount of ^{VI}Al corresponding to $Al(OH)_3$. The value of OH_x consists of two parts, one of which compensates the extra positive charge of Na, K, ^{IV}Al which is equal to $|(Na_\alpha + K_\beta) - {}^{IV}Al_\gamma| = |m|$, and the other part that is equal to $OH_y = OH_x - |m|$. The number of vacant tetrahedra is $\square_y = OH_y/4$. In the formula

426 the total negative charge (4 – 3x) is equal to that of the positive charge if the amount of Si is (1 – $\square_y$
427 –γ).
428
429 **Oxygen isotopic composition**
430 The oxygen isotopic composition of 14 studied samples (Table 5) shows $\delta^{18}O$ values of 24.9
431 to 29.4‰. Whilst the $\delta^{18}O$ value for sample 18at the most shallow depth (1963.52 m in Well M-10)
432 is the highest reported (29.4‰), and the two lowest measured$\delta^{18}O$ values (identical at 24.9‰) are at
433 the greatest depths (respectively 2794.3 and 2826.84m in Rigs-1), see Figure 12, we do not argue
434 that there is convincing evidence for either a systematic, or indeed stepwise, trend with depth: ten
435 $\delta^{18}O$ values within a narrow depth range of 2057.63 to 2135.8m have an analytically significant
436 $\delta^{18}O$ variation of 2.5‰ (26.4 to 28.9). Whilst the details of the $\delta^{18}O$ variations (e.g. with age and
437 syndepositional characteristics such as temperature, water $\delta^{18}O$ etc; and/or with post-depositional
438 effects) will likely prove informative, such consideration is beyond the remit of this paper, and so
439 we focus rather on first-order interpretation.
440 The overall mean of the 13 measured $\delta^{18}O$ values is 27.5±2.6‰ (1σ), and excluding the three
441 extreme values (see Figure 12) the ten remaining average to 27.8±0.9‰. These values are similar to
442 those for primary marine silica (26.6 to 27.7‰ for purified material) precipitated in the South Oman
443 Salt Basin at the Precambrian/Cambrian boundary (Ramseyer et al. 2013). Using the quartz-water
444 oxygen isotope fractionation calibration suggested by Matsuhisa et al. (1979), the argument is not
445 significantly affected if the amorphous silica calibration of Kita et al. (1985) is substituted, and
446 using an estimated seawater $\delta^{18}O$ of -1.2‰ on a deglaciated Earth (see Jaffres et al. (2007) for a
447 detailed review of seawater $\delta^{18}O$), then the temperature estimated from 27.8±0.9‰ is 48.5±4°C.
448 The ±4°C estimate of precision arises solely from propagation of the ±0.9‰ 1σ spread on measured
449 silica $\delta^{18}O$. On the question of accuracy, we note that a 1‰ decrease in the assumed seawater $\delta^{18}O$

would result in a temperature decrease of 4.8°C and that there is also an unquantified error arising from the assumed oxygen isotope equilibrium calibration. There are also issues on whether the measured silica $\delta^{18}O$ was established at the time of precipitation or during a subsequent oxygen isotope exchange process. Notwithstanding all of these concerns, the best-estimate of several tens of degrees Celsius (as opposed to estimates different by an order of magnitude, say) does not seem unreasonable at all for the Tertiary sea.

Discussion

Identification of the weak hydrogen absorption bands in the IR spectra

Defects related to $[4H]_{Si}$ hydrogarnet defects. The absorption bands at 3585 cm^{-1} were observed in the IR spectra of synthetic and natural quartz, amethyst (Kats 1962; Chakraborty and Lehmann 1976; Paterson 1982; Stalder and Konzett 2012; Stalder and Neuser 2013) and chalcedony (Frondel 1982). This band is assigned to the hydrous defect generated by substitution of Si^{4+} by $4H^{+}$ and is referred to as the $[4H]_{Si}$ or hydrogarnet defect. The highest intensity band is observed at 3588 cm^{-1} for all studied samples (Figure 9) showing that this defect plays the decisive role among all hydrogen defects in their structures. Application of first-principle calculations to investigate the atomic geometries and thermodynamic properties of water-related defects in α-quartz showed that the $[4H]_{Si}$ defect is thermodynamically most stable and aggregates to form platelets in the form of micro-cracks with hydroxylated surfaces on both their sides (Lin et al. 1994; McConnell et al. 1995; McConnell 1996; de Leeuw et al. 1999; Rosa et al. 2005). The origin of the other strong absorption band at 3613cm^{-1} in the IR spectra is not assigned in the literature although a weak band at 3615cm^{-1} together with a strong band at 3585 cm^{-1} was observed in the spectra of amethyst (Kats 1962) and chalcedony (Frondel 1982). One possible origin of the band at 3613cm^{-1}

is that the nano-quartz structure along with aggregation of $[4H]_{Si}$ defects forming a hydroxylated surface contains isolated $[4H]_{Si}$ defects (Figure 8a). According to calculations of Rosa et al. (2005) the formation of planar defects under thermodynamic equilibrium conditions is energetically more favorable than that of isolated $[4H]_{Si}$ defects. However, the formation of nano-quartz probably occurred under non-equilibrium conditions which may be favorable for the formation of isolated defects. Thus, the bands at 3588and 3613 cm^{-1} may correspond to the platelet and isolated $[4H]_{Si}$ defects, respectively. In this case, one has to assume that for isolated defects hydrogen bond lengths between H and O atoms should on average be longer as compared with those in the platelet defects providing the higher frequency for the isolated defects. The linear relationship between intensities of the absorption bands at 3588 and 3613 cm^{-1} observed for samples having different thicknesses can be considered as indirect evidence of their similar origin (Figure 10).

In general, these results are in agreement with the interpretation of the structural imperfections in nano-quartz samples obtained from the $^{29}Si\{^{1}H\}$CP/MAS NMR spectra (Figure 6). Indeed, the clear observation of the resonance at -107.4 ppm at different CP contact times is in accordance with the presence of $[4H]_{Si}$ defect sites, whereas the appearance of the resonance at -97.67 to -98.0 ppm shows that Si cations interact directly with the hydroxyls on the surface formed by hydrogarnet defects. The presence of two intense bands in the IR spectra is in agreement with two resonance peaks at -97.6 to -98.0 ppm and at -99.6 to -99.8 ppm, observed in the $^{29}Si\{^{1}H\}$CP/MAS NMR spectra of the nano-quartz samples. Both resonances originate from sites of the type $(Si–O)_3–Si^*–OH$ and are ascribed to Si neighboring the $[4H]_{Si}$ defects. The resonance at -97.6 to -98.0 ppm is clearly broader than the -99.6 to -99.8 ppm peak and it is tentatively assigned to the aggregated $[4H]_{Si}$ defects as a result of its larger linewidth and its shift towards higher frequency, the latter being expected for the more open structure around the aggregated defects as compared to the isolated defects. Thus, the narrow peak at lowest frequency (-99.6 to -99.8 ppm) is

498 ascribed to isolated $[4H]_{Si}$ defects. As will be shown below, these results are in accordance with
499 those following from the relationships between the *a* and *c* unit-cell parameters as well as between
500 the OH_y content and the unit-cell parameters. However, the assignment of the overlapping $(Si–O)_3$–
501 Si*–OH peaks is not unambiguous and will require further $^{29}Si\{^1H\}$CP/MAS NMR experiments,
502 e.g. on quartz samples where there is a clear distinction between aggregated and isolated $[4H]_{Si}$
503 defect sites.
504
505 **The IR region related with Al–H defects.** The characteristic feature of the IR spectra of
506 natural quartz is the presence of a strong absorption triplet at 3310 cm^{-1}, 3374$cm^{-1}$and 3440cm^{-1}
507 (Kats 1962; Bambauer 1963; Brown and Kahan 1975; Aines and Rossman 1984) which were
508 assigned to coupled substitutions Si^{4+} for Al^{3+} + H^+ forming so called Al–H defects. Based on the
509 orientation of the O-H vectors coordinated to tetrahedralAl^{3+}cations, Kats (1962) concluded that
510 there are two types of Al–H defects where one is related to the 3310cm^{-1} band and the other to the
511 pair of 3374 $cm^{-1}$and 3440 cm^{-1}bands. The first type of Al–H defects results from H^+ bound
512 between the two non-equivalent oxygen atoms in the Al^{3+}tetrahedron and the 3374 and 3440cm^{-1}
513 pair arises from OH^- group in the Al^{3+}tetrahedron with O-H vectors pointing into the *c* axis
514 "channel" forming an angle 75° with the *c* axis. Stalder and Konzett (2012) and Stalder and Neuser
515 (2013) investigated OH defects in detrital quartz grains and identified also the absorption triplet at
516 3310 cm^{-1}, 3378$cm^{-1}$and 3430cm^{-1}. In the IR spectra of the studied samples, the absorption band at
517 3378 cm^{-1} corresponding to an Al–H defect is partially overlapped with an absorption band at 3384
518 cm^{-1} of Na related to an OH defect (Aines and Rossmann 1984). Positions of the sharp bands, at
519 3440 and 3330cm^{-1}, are clearly distinguishable and according to Chakraborty and Lehman (1976)
520 the 3440cm^{-1}band should correspond to H^+ bonded directly to Si^{4+} whereas the band at 3430 cm^{-1}corresponds to an Al–H defect. In different IR spectra of the studied samples two wide bands at

3430 and 3440 cm^{-1}appear with different occurrence probability and the resulting position of the overlapping bands varied from 3436 to 3444 cm^{-1} (Figure 9). Finally, according to Muller and Koch-Muller (2009) and Baron et al. (2015) the Li-specific OH absorption band is located at 3480 cm^{-1} and 3483 cm^{-1}, respectively. Therefore, the origin of the very weak band at 3473–3474 cm^{-1} occasionally observed in the studied spectra probably has the same origin.

The relationship between the nature and location of the charge-compensation ions and the features of the IR spectra. Aluminum is the most common trace element in natural and synthetic quartz samples and other impurity elements (e.g. H, Na, Li, K) are incorporated in quartz structures to compensate the negative charge originating from substitution of Si^{4+} by Al^{3+}in the tetrahedral sites of the quartz framework. The charge compensation usually takes place by formation of local structural arrangements, $[AlO_4/M^+]^o$ defects ($M^+ = H^+$, Na^+, Li^+, and K^+), which according to Botis and Pan (2009) are stable in the quartz structure. Therefore, in natural quartz tetrahedral Al stands generally in an approximately stoichiometric relation to the content of (OH) and trace alkalis (Botis and Pan 2009).

The analysis of the IR spectra of the studied samples shows some unusual relationships between IR particular features and location of the cation compensators. To demonstrate this, let us consider at first the relationship between the amount of tetrahedral Al^{3+}cations, C_{Al}, and the total content of Na^+ and K^+, $C_{(Na+K)}$, in the structural formulae (Figure 13, Table 4). All samples can be divided into three groups: in one of them $C_{Al} > C_{(Na+K)}$, in the other $C_{Al} < C_{(Na+K)}$, and in the last one $C_{Al} = C_{(Na+K)}$ (Figure 13). In sample 19 (E-5, 2078.74) of the first group the content of $C_{(Na+K)}$ is negligible (0.0003) in comparison to that of C_{Al} (0.0030). One could expect that the IR spectrum of the sample would contain strong absorption bands corresponding to Al–H defects. In contrast, the intensity modulations observed in the diagnostic region (3200–3500 cm^{-1}) of the spectrum can

546 hardly be distinguished from the background. To explain the observed inconsistency, one has to
547 take into account that some of the studied samples contain local structural fragments in which a
548 negative charge generated by substitution of Si^{4+} for Al^{3+} is compensated by hydration of Si^{4+}
549 placed in the second coordination sphere of ^{IV}Al (Figure 8b). Therefore, the IR spectrum of sample
550 19 (E-5, 2078.74) does not contain absorption bands related to Al–H defects. This way of local
551 charge compensation assists the interpretation of particular features in the IR spectra of samples 9
552 (Sif-1, 2070.94) and 18 (M-10, 1963.52), both of which have almost the same amounts of ^{IV}Al and
553 (Na + K), respectively, equal to 0.0019 and 0.0028 for the first and 0.0018 and 0.0026 for the
554 second sample (Table 4). In contrast, the IR spectra of the samples differ from each other by the
555 distribution of intensities of the absorption bands in their diagnostic regions. The IR spectrum of
556 sample 18 (M-10, 1963.52) is quite similar to that of sample 19 (E-5, 2078.74) because the
557 intensities of the bands in the diagnostic region are negligibly small. In contrast, the characteristic
558 absorption bands at 3378 and 3440 $cm^{-1}$are clearly distinguishable in the spectrum of sample 9 (Sif-
559 1, 2070.94) (Figure 9). To explain these observations, one has to take into account, that according to
560 Botis and Pan (2009) the structure of both samples contains local $[AlO_4/(Na + K)]^o$ defects and that
561 the amount of these should be equal to the content of (Na + K) in each sample. In the compared
562 samples the tetrahedral Al^{3+} cations, whose amount is equal to $C_{Al} - C_{(Na+K)}$,may have different local
563 positions. In sample 18 (M-10, 1963.52) the charge compensation most probably took place
564 according to the local environment shown in Figure 8 where an OH^- group coordinated one of the
565 four tetrahedral Si^{4+} closely located to the Al^{3+}tetrahedron. Therefore, the diagnostic region of the
566 IR spectrum of sample 18 (M-10, 1963.52) is similar to that of sample 19 (E-5, 2078.74) (Figure 8).
567 In contrast, in samples 9 (Sif-1, 2070.94) and 14 (Sif-1, 2088.3) the negative charge originating
568 from the tetrahedral Al^{3+}cations remaining after formation of electroneutral structural arrangements

569 $[AlO_4/Na^+]^o$ were compensated by formation of Al–H defects. As a result, in the IR spectra of both
570 samples the absorption bands corresponding to Al–H defects are observed (Figure 9).
571 Interpretation of the IR spectra of the flint samples is not always unambiguous. As mentioned
572 earlier, for determination of the chemical composition of these samples, raw material was used and
573 probably some amount of Na was adsorbed from the pore water. Because of this uncertainty, the
574 influence on IR effects of a high concentration of NaOH + KOH in some of the studied samples
575 was not unequivocally solved within the frame of this study.
576
577 **Unit cell parameters of nano-quartz samples as indicators of their main structural**
578 **imperfections.**
579 **Comparison of the unit cell parameters of nano-quartz and well crystallized quartz.** The
580 main feature of the nano-quartz is that tetrahedral vacancies constitute up to 0.03 per 2 anions,
581 whereas Al^{3+} occupies less than 0.006 per 2 anions of the tetrahedral sites (Table 4) and OH^-
582 amounts to up to 0.112 per 2 anions. The tetrahedral vacancies with $4OH^-$ anions adjacent are
583 therefore for the nano-quartz the most significant deviation from the ideal formula for α-quartz and
584 the main contributors to the deviation of the unit cell parameters from those of well-crystallized
585 natural quartz. The cell dimensions of the nano-quartz from the chalk and the flint are significantly
586 larger (4.9164 to 4.9195 Å for the *a*-parameter and from 5.4047 to 5.4097 Å for the *c*-parameter,
587 Table 1) than the dimensions of natural and synthetic quartz being 4.9121 – 4.9149 Å for the *a* cell
588 parameter and from 5.4038 – 5.4054 Å for the *c* cell parameter (Table 6) (Cohen and Sumner 1958;
589 Afanas'eva et al. 1960; Hurst and Storch 1981).The presence of tetrahedral vacancies and Al^{3+} ions
590 replacing Si^{4+} should result indistinct $(Si–O)_3–Si^*–OH$ and $(Si–O)_3–Si^*–O–Al$ resonances in the
591 single-pulse ^{29}Si MAS NMR spectra (Figure 5). ^{29}Si spin-lattice relaxation times of T1 = 3000 –
592 4000 s have been reported for forα-quartz at ambient temperature (Spearing et al. 1992), implying

593 the single-pulse ^{29}Si MAS NMR spectra in Figure 5 only detects a very small fraction of the total
594 intensity (15 - 19 %), considering the actual experimental conditions (45^{o} excitation pulse, 300 s
595 relaxation delay). Thus, the absence of clear resonances from^{29}Sineighbouring the defects in nano-
596 quartz is tentatively ascribed to very long relaxation times for these sites. However, the resonances
597 from the $[4H]_{Si}$ defects, $(Si–O)_3–Si^*–OH$ sites, are clearly seen at -97.6 to -99.8 ppm in the
598 $^{29}Si\{^1H\}$ CP/MAS NMR spectra, reflecting the fact that the intensity in these experiments are
599 dependent on the ^{1}H spin-lattice relaxation which is generally orders of magnitude faster than the
600 ^{29}Si spin-lattice relaxation for silicate minerals (Skibsted et al. 1995).
601
602 **Space orientation of platelets formed by aggregated $[4H]_{Si}$ defects.** As was mentioned,
603 McLaren et al. (1983) suggested that hydrogen is incorporated in the wet quartz structure as $[4H]_{Si}$
604 defects. On heating these defects migrated toward each other to form clusters. According to the
605 TEM experiments of McLaren et al. (1983), the increase in temperature transformed the aggregated
606 $[4H]_{Si}$ defects into bubbles of high pressure water fluid lying on dislocation loops with Burgers
607 vector b=a/3 $\langle 11\bar{2}0\rangle$ parallel to the $(0\bar{1}10)$or$(10\bar{1}0)$planes. This model was partly reconsidered by
608 Lin et al. (1994), McConnell et al. (1995) and McConnell (1996) who supposed that at a high $[4H]_{Si}$
609 concentration in wet quartz these defects segregate to form planar precipitate rafts or platelets lying
610 in the $(0\bar{1}10)$ plane (Figure 7). In contrast, the simulation results of de Leeuw et al. (1999) showed
611 that aggregation of $[4H]_{Si}$ defects forming the (0001) OH surface is more stable than those forming
612 the $(10\bar{1}0)$, $(10\bar{1}1)$, and $(10\bar{1}\bar{1})$ OH surfaces. Rosa et al. (2005) also analyzed thermodynamic
613 properties of a quartz containing platelets of $[4H]_{Si}$ defects lying in the $(0\bar{1}10)$ plane and found that
614 platelets lying in this plane are less stable than the platelets in the (0001) plane (Figure 14).
615 Moreover, Rosa et al. (2005) considered the influence of dilation of the lattice parameters *a* and *c*
616 on the structural and energetic properties of the platelet defects. It was found that for the atomic

configuration in which the platelets lie in the (0001) plane, relaxation of the *a* parameter has negligible effect on the formation energies and the geometry. In contrast, the final most stable atomic geometry was accompanied by increasing the *c*-parameter. At the same time, these authors emphasized that their calculations were carried out assuming thermodynamic equilibrium. Therefore, they do not discard the possibility that the $(0\bar{1}10)$ platelets may be kinetically stabilized. It seems plausible that the studied nano-quartz samples were formed in thermodynamically non-equilibrium conditions. The results obtained by MAS NMR and IR spectroscopic methods in this work are in agreement with the presence of hydroxylated surfaces formed by the aggregated $[4H]_{Si}$ defects but their space orientation in nano-quartz remains uncertain. To solve this problem one has to take into account that the size of the $[4H]_{Si}$ structural unit is larger than the SiO_4 unit. Therefore, it is likely that the replacement of Si by 4H in the same oxygen framework should provide preferential expansion of the lattice along the normal to the platelets formed by aggregated $[4H]_{Si}$ defects, that is either to the (0001) or $(0\bar{1}10)$ planes.

Relationships between *a*- and *c*-parameters. The *a*- and *c*-parameters of most samples follow a linear interdependence, but the positions of some of the samples deviate significantly from the linear regression (Figure 15). However, the positional distribution of these samples has some particularly interesting features. The most remarkable one is that the positions for about 50% of the samples (all of which are flints) are located along the grey line almost parallel to the *c* axis (i.e. the abscissa) from sample 3 (Rigs-1, 2826.84) having lower *c* value to sample 7 (Sif-1, 2065.0) having higher *c* value (Figure 15). These samples have practically the same *a* values, from 4.9169 Å (sample 3) to 4.9171 Å (sample 7) (Table 1, Figure 15). In contrast, the *c* values for this set of samples increase from 5.4047 Å to 5.4071 Å, that is by up to 0.0024 Å. Similarly, samples 18 (M-10, 1963.52) and 11 (Sif-1, 2071.11) have almost the same *a* value (4.9164 and 4.9166 Å) whereas

641 the *c* value of the parameter of sample 11 (5.4072 Å) is higher than that of sample 18 (5.4059 Å) by
642 0.0013Å (Table 1, Figure 15). Among the samples deviating strongly from the linear regression is
643 sample 10 (Sif-1, 2071.08) which is also unusual with respect to its cation composition. According
644 to the chemical formula of sample 10, the content of (Na + K) (0.0145) is 3 to 10 times higher than
645 those in other samples (Table 4). The high content of (Na + K) cations, which are located into
646 channels of the quartz structure, strongly increases the *a*-parameter value of the sample (Afanas'eva
647 et al. 1960). For this reason the position ofsample10falls far from those of the other samples (Figure
648 15).

649 For idealized equilibrium conditions the formation of platelets lying parallel to the (0001)
650 plane should increase only the *c*-parameter. The tendency of increasing *a*-parameter observed in
651 Figure 15 may be due to the following: first, possible isolated $[4H]_{Si}$ defects should increase the cell
652 volume homogeneously in different crystallographic directions. On the other hand, different
653 contents and distributions of structural defects related to tetrahedral Al^{3+}, H^{+}, Na^{+}, and K^{+}
654 impurities have different influence on the unit cell parameters. Nevertheless, the regularities in the
655 relationships between the *a*- and *c*-parameters, observed in Figure 15, can be considered as
656 independent evidence that the planar defects of hydrogen atoms in the nano-quartz are parallel to
657 the (0001) plane. Knowledge of the space orientation of the aggregated $[4H]_{Si}$ defects, the presence
658 of two strong absorption bands at 3588 and 3613 cm^{-1} and the relationship between their intensities
659 (2:1) allows us to assume that these two bands correspond to two different types of $[4H]_{Si}$ defects in
660 a nano-quartz structure. In one type, aggregated $[4H]_{Si}$ defects form OH surfaces parallel to (0001)
661 plane (Figure 14) whereas in the second type the $[4H]_{Si}$ defects is probably represented by
662 individual hydrogarnet defects (Figure 8a).
663

664 **Direct evidence of decisive and selective influence of $[4H]_{Si}$ defects on the unit cell**
665 **parameters of nano-quartz.** The origin of the main regularities between the *a* and *c* parameters of
666 the unit cells of the studied samples becomes more clear from the analysis of the relationships
667 between the unit cell parameters and amounts of OH^- groups, designated OH_y, forming $[4H]_{Si}$
668 defects (Tables 1 and 4). At first let us consider some features observed between the *a*-parameters
669 and the OH_y values. As can be seen in Figure 16a for the majority of the samples, the *a*-parameter
670 values are almost independent of the OH_y. Indeed, the *a*-parameter of a subset of samples 3, 8, 13, 7
671 and 14 varies in the very narrow interval from 4.9169 to 4.9172 Å, whereas the OH_y values increase
672 from 0.0152 to 0.0699 (Tables 1, 4, Figure 16a). In contrast, as can be seen in Figure 16b for the
673 same set of samples, values of the *c*-parameter increase significantly from 5.4047 to 5.4071 Å. This
674 means, first, that the higher the OH_y value the higher value of the *c*-parameter and, second, that
675 most probably the majority of $[4H]_{Si}$ defects were formed as aggregated platelets parallel to the
676 (0001) plane. These conclusions are in agreement with the relationship between the *a*- and *c*-
677 parameters for the samples according to which the increase of the *c*-parameter may occur at the
678 same time as values of the *a*-parameter are within error (Figure 15). Similarly, the mutual
679 relationship between the unit cell parameters and the OH_y values is observed for the pair of the
680 samples 18 and 11 whose *a*-parameters are almost the same (4.9164 and 4.9166 Å) whereas the
681 content of OH_y in sample 11 (0.0565) is higher than that (0.0460) in sample 18 (Figure 16a). In
682 agreement with the regularity mentioned above, the *c*-parameter of sample 18 (5.4059 Å) is lower
683 than that of sample 11 (5.4072 Å) (Figure 16b).
684 The amount of OH_y may also control the *c*-parameter for the nano-quartz samples having
685 different values of the *a*-parameter. For example, samples 18 and 8 have different *a*-parameters
686 (4.9164 and 4.9171 Å), close amounts of OH_y (0.0460 and 0.0408) and identical *c* values (5.4059
687 and 5.4058 Å) (Figure 15). The difference between the *a*-parameters in these samples is due to a

688 high amount of K^+ (0.0010) in the total amount of alkaline cations (0.0022) in sample 8 relative to
689 the content of the Na^+ cations in sample 18 (0.0018). Moreover, in sample 8 $C_{(K+Na)} > C_{Al}$ whereas
690 $C_{Al} > C_{(Na+K)}$ in sample 18 (Table 4). Therefore, the high amount of KOH and NaOH structural units
691 located in the structural channels causes the higher value of the *a*-parameter in sample 8 in
692 comparison with that of sample 18. However, similar values for OH_y in these samples result in
693 almost the same values of their *c*-parameters (Figure 16b). The results described are in agreement
694 with the interrelations between the *a*- and *c*-parameters of samples 8 and 18 (Figure 15).
695 An even more remarkable selective influence of $[4H]_{Si}$ defects on the *a* and *c* unit cell
696 parameters for nano-quartz is seen from the comparison of the unit cell parameters and chemical
697 composition of samples 12 and 10. As mentioned previously these samples differ from each other
698 by the amounts of alkaline cations ($C_{(K+Na)}$ = 0.0020 and 0.0120) and tetrahedral Al^{3+}cations
699 (0.0024 and 0.0060). As a result, the *a*-parameter of sample 10 (4.9195 Å) is higher than that of
700 sample 12 (4.9186 Å) (Figure 16a). However, a similar content of OH_y (0.1118 and 0.0959) and,
701 thus, vacant tetrahedral sites in samples 12 and 10 (0.0279 and 0.0240) results in similar values of
702 their *c*-parameters (Figure 16b).
703 To summarize the observed correlations between the unit cell parameters, the amount of OH_y
704 groups, and the theoretical predictions concerning the orientation of the aggregated platelets can be
705 considered as direct evidence that the amount of water released during heating of the studied
706 samples does correlate with the amount of OH_y groups in the calculated formulae of the samples.
707 This conclusion is not in conflict with the structural features ofsamples19and 18which do not
708 follow the relationships between the unit cell parameters and the amount of $[4H]_{Si}$ defects found for
709 the other samples. Indeed, these samples contain similar amounts of OH_y (0.0435 and 0.0460) but
710 have different *c*-parameters (5.4069 and 5.4059 Å). One plausible explanation of the observed
711 deviation may be related to the rather high content of tetrahedral Al^{3+} (0.0030) and the negligible

amount of alkaline cations in sample 19 (Table 4). Moreover, the IR spectrum of this sample does not contain absorption bands responsible for Al–H defects (Figure 9). This means that the tetrahedral Al^{3+} cations in sample 19 are coordinated by only oxygen atoms and excess negative charge is compensated by OH hydroxyls each of which coordinates one of the four Si cations nearest to the AlO_4 tetrahedron (Figure 8b). Because the volume of the AlO_4 structural unit is larger than that of a SiO_4 unit and because the amount of tetrahedral Al^{3+} cations in the structure is significant (0.0030), not only the *a*- (4.9174 Å) but also the *c*- (5.4069 Å) parameter of sample 19 are higher than those of sample 18 (4.9164 and 5.4059 Å).

Sample 17 is the only example whose crystal-chemical composition does not correlate with the *c*-parameter value. According to the formula, the content of OH_y in sample 17 (0.1040) is similar to those in samples 12 (0.1118) and 10 (0.0959) (Figure 15). Therefore, one may expect that the *c*-parameters of samples 17, 12, and 10 should have similar values. In contrast, this expectation is met only for samples 12 and 10 (c = 5.4096 and 5.4097 Å), whereas the c value for sample 17 is much lower and equal to 5.4068 Å. One possible reason for the observed discrepancy is that the particles in sample 17 along with the $[4H]_{Si}$ defects contain some amount of water molecules located in small bubbles, released from the sample at relatively high temperature.

A general remark concerning the formation of nano-quartz

The fact that quartz is almost pure SiO_2 makes an accurate determination of elements other than Si difficult. The amount of structural impurities has previously been estimated based on interpretation rather than on determination, and the correlation between local structural imperfections and unit cell parameters has consequently been beset with uncertainties (Hurst and Storch 1981).

735 In the present investigation of the nano-quartz the application of XRD, IR, and ^{29}Si and ^{27}Al
736 MAS NMR together with thermal analysis of released H_2O and elemental analysis by AAS makes it
737 possible to characterize the nano-quartz structure much more accurately. The main feature of the
738 structure is that tetrahedral vacancies constitute up to 5% of the tetrahedral sites or up to 0.03 per 2
739 anions, whereas Al^{3+} occupies less than 1% of the tetrahedral sites or up to 0.006 per 2 anions
740 (Table 4). OH^- amounts up to 0.0112 per 2 anions. The tetrahedral vacancies with 4 OH^- anions
741 adjacent are therefore, for the nano-quartz, the most significant deviation from the ideal formula for
742 α-quartz.
743 Laboratory experiments have shown that quartz can be synthesized from sea water at room
744 temperature (Mackenzie and Gees 1971). The new model for the formation of nano-quartz in flint
745 and as nano-quartz particles dispersed in the chalk during sedimentation (Lindgreen et al. 2011;
746 Lindgreen and Jakobsen 2012) is in agreement with a low temperature of formation, as inferred
747 from the isotopic data. The quartz dispersed in the chalk and the quartz in the flint have almost
748 identical unit cell parameters, strain values and sizes of CSD's and this demonstrates that the quartz
749 in the chalk and in the flint have formed by the same mechanism (Lindgreen et al. 2011).
750 The formation by crystallization in the sea, the spherical nano-particles and the larger cell
751 dimensions make the North Sea nano-quartz a type of quartz totally different from the well-
752 crystalline quartz of hydrothermal, magmatic or metamorphic origin. This is in agreement with the
753 absence of a sharp α→β transition exothermic peak in DTA, which is due to the nano-size of the
754 quartz crystals (Rios et al. 2001), whereas normal quartz has been characterized by having a sharp
755 α→β peak at 573°C (Dawson and Wilburn 1970).
756

757 **Implications**

Quartz is the most abundant mineral on the Earth's surface and is usually characterized and identified from its particle shape, the low-angle part of the XRD pattern and an elemental composition as SiO_2. As an example, the quartz in the chalk reservoirs of the oil fields of the North Sea has so far been identified and quantified from XRD patterns in the 10– 40 °2θ range. Our application of different methods, allowing us to reveal the finest features at the nano-structural level, has demonstrated that the quartz structure is much more variable than hitherto assumed and that the application of nano-structural methods can discover totally new structures and lead to the understanding of new mechanisms for the formation of quartz at low temperature from biogenic silica, and perhaps eventually reveal specific geochemical conditions in the marine environment resulting in the sedimentary formation of flint.

The new form of quartz, the nano-size spherical α-quartz, is the only silica mineral observed in the Danian chalk in the oil well cores investigated. It has previously been concluded that the quartz formed by crystallization in the water column from dissolved radiolarian organisms. The fact that the nano-quartz has significantly larger dimensions compared to normal quartz and that the elemental structure is special in having a significant proportion of ^{IV}Al substituting for Si and of $[4H]_{Si}$ hydrogarnet defects means that the conditions for formation of this quartz had a strong impact on its structure. The size of the quartz particles makes them effective in packing between coccolithic chalk particles and may cause decreased porosity and permeability in the oil reservoirs, for example contributing to the tight character of the lower part of the Danian Ekofisk Formation. The porous structure of the flint consisting of sedimented quartz spheres makes saturation of the flint with oil during reservoir filling possible and thus reflects the timing of oil migration in the reservoirs (Jakobsen et al. 2014). Investigations should detect this special form of quartz by recording XRD patterns in the high-angle region where the character of this quartz mineral is revealed.

782

783 **Acknowledgements**

784

785 We are grateful to E.V. Pokrovskaya for her help in the Ms preparation. J. Skibsted
786 acknowledges the Carlsberg Foundation for an equipment grant. SUERC is supported by a
787 Consortium of Scottish Universities. V.A. Drits and O. Dorzhieva acknowledge the support of
788 budget project #0135-2016-0010.

789

790 **References cited**

791 Aines, R., and Rossman, G.R. (1984) Water in minerals? A peak in the infrared. Journal of
792 Geophysical Research, 89, 4059-4071.
793 Afanas'eva, N.A., Kamentsev, I.E., and Frank-Kamenetskii, V.A. (1960) Variation of the
794 elementary cell parameters of quartz of different sources. Soviet Crystallography, 4,
795 354-357.
796 Andersen, M.D., Jakobsen, H.J., and Skibsted, J. (2006) A new aluminium-hydrate species in
797 hydrated Portland cements characterized by ^{27}Al and ^{29}Si MAS NMR spectroscopy.
798 Cement and Concrete Research, 36, 3–17.
799 Bambauer, H.U. (1963) Merkmale des OH-spectrums alpine quarze (3 μ-Gebiet). Schweizerische
800 Mineralogische und Petrographische Mitteilungen, 43, 259-268.
801 Baron, M.A., Stalder, R., Konzett, J., and Hauzenberger, C.A. (2015) OH-point defects in quartz in
802 B- and Li-bearing systems and their application to pegmatites. Physics and Chemistry
803 of Minerals, 42, 53-62.
804 Beran, A., and Libowitzky, E. (2003) IR spectroscopic characterization of OH defects in mineral
805 phases. Phase Transitions, 76, 1-15.
806 Bernas, B. (1968) A new method for decomposition and comprehensive analysis of silicates by
807 atomic absorption spectroscopy. Analytical Chemistry, 40, 1682-1686.
808 Botis, S.M., and Pan, Y. (2009) Theoretical calculation of $[AlO_4/M^+]^0$ defects in quartz and crystal
809 chemical controls on the uptake of Al. Mineralogical Magazine, 73, 537-550.
810 Brice, J.C. (1980) The lattice constants of a-quartz. Journal of Materials Science, 15, 161-167.
811 Bromley, R.G., and Ekdale, A.A. (1986) Flint and fabric in the European Chalk. In: G.D.G.
812 Sieveking and M.B. Hart, Eds., The Scientific Study of Flint and Chert, 71-82,
813 Cambridge University Press, Cambridge.

814 Brown, R.N., and Kahan, A. (1975) Optical absorption of irradiated quartz in the near IR. Journal of
815 Physics and Chemistry of Solids, 36, 467-476.
816 Chakraborty, D., and Lehmann, G. (1976) Distribution of OH in synthetic and natural quartz
817 crystals. Journal of Solid State Chemistry, 17, 305-311.
818 Clayton, C.J. (1986) The chemical environment of flint formation in Upper Cretaceous chalk. In:
819 G.D.G. Sieveking and M.B. Hart, Eds., The Scientific Study of Flint and Chert, 43-54.
820 Cambridge University Press, Cambridge.
821 Cohen, A.J., and Sumner, G.G. (1958) Relationships among impurity contents, color centers and
822 lattice constants in quartz. American Mineralogist, 43, 58-68.
823 Cordier, P., Weil, J.A., Howarth, D.E., and Doukhan, J.C. (1994) Influence of the $(4H)_{Si}$ defect on
824 dislocation motion in crystalline quartz. European Journal of Mineralogy, 6, 17-22.
825 Dawson, J.B., and Wilburn, F.W. (1970) Silica minerals. In R. C. Mackenzie, Ed., Differential
826 Thermal Analysis, Vol. 1, 477-497. Academic Press, London.
827 Dennen, W.H. (1966) Stoichiometric substitution in natural quartz. Geochimica et Cosmochimica
828 Acta, 30, 1235-1241.
829 Dennen, W.H., and Blackburn, W.H. (1970) Aluminum in quartz as a geothermometer.
830 Contributions to Mineralogy and Petrology, 27, 332-342.
831 Frondel, C. (1982) Structural hydroxyl in chalcedony (Type B quartz). American Mineralogist, 67,
832 1248-1257.
833 Götze, J., Plötze, M., Raupner, T., Hallbauer, D.K., and Bray, C.J. (2004) Trace element
834 incorporation into quartz: A combined study by ICP-MS, electron spin resonance,
835 cathodoluminescence, capillary ion analysis, and gas chromotography. Geochimica et
836 Cosmochimica Acta, 68, 3741-3759.
837 Holmes, A. (1965) Principles of Physical Geology. Thomas Nelson and Sons, London, 2nd Edition.

838 Hurst, V.J., and Storch, S.P. (1981) Regional variation in the cell dimensions of metamorphic
839 quartz. American Mineralogist, 66, 204-212.
840 Jaffres, J.B.D., Shields, G.A., and Wallmann, K. (2007) The oxygen isotope evolution of sea water:
841 A critical review of a long-standing controversy and an improved geological water
842 cycle model for the past 3.4 billion years. Earth-Science Reviews, 83, 83-122.
843 Jakobsen, F., Lindgreen, H., and Springer, N. (2000) Precipitation and flocculation of spherical
844 nano silica in North Sea chalk. Clay Minerals, 35, 175-184.
845 Jakobsen, F., Lindgreen, H., and Nytoft, H.P. (2014) Oil-impregnated flint in Danian chalk in the
846 Tyra field, North Sea Central Graben. Journal of Petroleum Geology, 37, 43-54.
847 Kamentsev, I.Y. (1965) Effect of temperature of crystallization on entry of aluminum into structure
848 of natural quartz. Geochemistry International USSR, 2, 237.
849 Kats, A. (1962) Hydrogen in alpha quartz. Philips Research Reports, 17, 133-279.
850 Kita, I., Tagutchi, S., and Matsubaya, O. (1985) Oxygen isotope fractionation between amorphous
851 silica and water at 34-93°C. Nature, 314, 83-84.
852 de Leeuw, N.H., Higgins, F.M., and Parker, S.C. (1999) Modeling the surface structure and stability
853 of α-quartz. The Journal of Physical Chemistry, 103, 1270-1277.
854 Lin, J.S., Payne, M.C., Heine, V., and McConnell, J.D.C. (1994) Ab initio calculations on $(OH)_4$
855 defects in α-quartz. Physics and Chemistry of Minerals, 21, 150-155.
856 Lindgreen, H., Jakobsen, F., and Springer, N. (2010) Nano-size quartz accumulation in reservoir
857 chalk, Ekofisk Formation, South Arne Field, North Sea. Clay Minerals, 45, 171-182.
858 Lindgreen, H., Drits, V.A., Salyn, A.L., Jakobsen, F., and Springer, N. (2011). Formation of flint
859 horizons in North Sea chalk through marine sedimentation of nano-quartz. Clay
860 Minerals, 46, 525-537.

Lindgreen, H., and Jakobsen, F. (2012) Marine sedimentation of nano-quartz forming flint in North Sea Danian chalk. Marine and Petroleum Geology, 38, 73-82.

Lippmaa, E., Mägi, M., Samoson, A., Engelkhardt, G., and Grimmer, A.-R. (1980) Structural studies of silicates by solid-state high-resolution ^{29}Si NMR. Journal of American Chemical Society, 102, 4889-4893.

Macaulay, C.I., Fallick, A.E., Haszeldine, R.S., and Graham, C.M. (2000) Methods of laser-based stable isotope measurement applied to diagenetic cements and hydrocarbon reservoir quality. Clay Minerals, 35, 313-322.

Mackenzie, F.T., and Gees, R. (1971) Quartz: Synthesis at earth-surface conditions. Science, 173, 533-535.

Madsen, H.B., and Stemmerik, L. (2010) Diagenesis of flint and porcellanite in the Maastrichtian chalk at Stevns Klint, Denmark. Journal of Sedimentary Research, 80, 578-588.

Matsuhisa, Y., Goldsmith, J.R., and Clayton, R.N. (1979) Oxygen isotope fractionation in the system quartz-albite-anorthite-water. Geochimica et Cosmochimica Acta, 43, 1131-1140.

McConnell, J.D.C., Lin, J.S., and Heine, V. (1995) The solubility of $[4H]_{Si}$ defects in α-quartz and their role in the formation of molecular water and related weakening on heating. Physics and Chemistry of Minerals, 22, 357-366.

McConnell, J.D.C. (1996) Ab initio studies on water related species in quartz and their role in weakening under stress. Phase Transitions, 61, 19-39.

McLaren, A.C., Cook, R.F., Hyde, S.T., and Tobin, R.C. (1983) The mechanisms of the formation and growth of water bubbles and associated dislocation loops in synthetic quartz. Physics and Chemistry of Minerals, 9, 79-94.

Millot, G. (1970). Geology of Clays. Springer Verlag, London.

885 Moore, D.M., and Reynolds, R.C. (1997) X-ray diffraction and the Identification and Analysis of
886 Clay Minerals. Oxford University Press, Oxford.
887 Morgan, D.J. (1977). Simultaneous DTA-EGA of minerals and natural mineral admixtures. Journal
888 of Thermal Analysis, 12, 245-263.
889 Müller, A., and Koch-Müller, M. (2009) Hydrogen speciation and trace element contents of
890 igneous, hydrothermal and metamorphic quartz from Norway. Mineralogical
891 Magazine, 73, 569-583.
892 Paterson M. (1982) The determination of hydroxyl by infrared absorption in quartz, silicate glasses
893 and similar materials. Bulletin de la Societe Francaise de Minéralogie, 105, 20-29.
894 Ramseyer, K., Amthor, J.E., Matter, A., Pettke, T., Wille, M., and Fallick, A.E. (2013) Primary
895 silica precipitate at the Precambrian/Cambrian boundary in the South Oman Salt
896 Basin, Sultanate of Oman. Marine and Petroleum Geology, 39, 187-197.
897 Rios, S., Salje, E.K.H., and Redfern, S.A.T. (2001) Nanoquartz vs. macroquartz: a study of the
898 α↔β phase transition. European Physical Journal B, 20, 75-83.
899 Rosa, A.L., El-Barbary, A.A., Heggie, M.I., and Briddon, P.R. (2005) Structural and
900 thermodynamic properties of water related defects in α-quartz. Physics and Chemistry
901 of Minerals, 32, 323-331.
902 Sanz, J. (1990) Distribution of ions in phyllosilicates by NMR spectroscopy. In: Montano, A.,
903 Burragato, F. Eds. Absorption Spectroscopy in Mineralogy. Elsevier, Amsterdam, pp
904 103-144.
905 Sanz, J., and Serratosa, J.L. (1984) ^{29}Si and ^{27}Al high resolution MAS-NMR spectra of
906 phyllosilicates. Journal of the American Chemical Society, 106, 4790-4793.
907 Segnit, E.R., Stevens, T.J., and Jones, J.B. (1965) The role of water in opal. Journal of the
908 Geological Society of Australia, 12, 211-226.

909 Sharp, Z.D. (1990) A laser-based microanalytical method for the in situ determination of oxygen
910 isotope ratios of silicates and oxides. Geochimica et Cosmochimica Acta, 54, 1353-
911 1357.
912 Shinoda, K., and Aikawa, N. (1993) Polarized infrared absorbance spectra of an optically
913 anisotropic crystal: Application to the orientation of the OH^- dipole in quartz. Physics
914 and Chemistry of Minerals, 20, 308-314.
915 Skibsted, J., Jakobsen, H.J., and Hall, C. (1994) Direct observation of aluminium guest ions in the
916 silicate phases of cement minerals by ^{27}Al MAS NMR spectroscopy. Journal of the
917 Chemical Society Faraday Transactions, 90, 2095 – 2098.
918 Skibsted, J., Hjorth, L., and Jakobsen, H.J. (1995) Quantification of Thaumasite in Cementitious
919 Materials by $^{29}Si\{^1H\}$ Cross-Polarization Magic-Angle Spinning NMR Spectroscopy.
920 Advances in Cement Research, **7**, 69–83.
921 Spearing, D.R., and Stebbins, J.F. (1989) The^{29}Si NMR shielding tensor in low quartz. American
922 Mineralogist, 74(7-8), 956-959.
923 Spearing, D.R., Farnan, I., and Stebbins, J.F. (1992) Dynamics of the α-β Phase Transitions in
924 Quartz and Cristobalite as Observed by In-Situ High Temperature ^{29}Si and ^{17}O NMR.
925 Physical Chemistry of Minerals 19, 307 – 321.
926 Stalder, R., and Konzett, J. (2012) OH defects in quartz in the system quartz-albite-water and
927 granite-water between 5 and 25 kbar. Physics and Chemistry of Minerals, 39, 817-827.
928 Stalder, R., and Neuser, R.D. (2013) OH-defects in detrital quartz grains: Potential for application
929 as tool for provenance studies and overview over crustal average. Sedimentary
930 Geology, 294, 118-126.

931 Takahashi, T., Kanehashi, K., and Saito, K. (2008) First evidence of multiple octahedral Al sites in
932 Na-montmorillonite by ^{27}Al multiple quadrupole MAS NMR. Clays and Clay
933 Minerals, 56, 520-525.
934 Tanaka, M., and Makino, Y. (1998) Finite size effects in submicron barium titanate particles.
935 Ferroelectric Letters, 24, 13-23.
936 Zijlstra, H.J.P. (1987) Early diagenetic silica precipitation, in relation to redox boundaries and
937 bacterial metabolism, in Late Cretaceous chalk of the Maastrichtian type locality.
938 Geologieen Mijnbouw, 66, 343-355.
939 Weil J.A. (1975) The aluminum centers in α-quartz. Radiation effects, 26, 261-265.
940 Weil J.A. (1984) A Review of Electron Spin Spectroscopy and Its Application to the Study of
941 Paramagnetic Defects in Crystalline Quartz. Physics and Chemistry of Minerals, 10,
942 149-165.
943

List of figure captions

Figure 1: Photos of cores from well Sif-1. Positions of chalk samples 11(Sif-1,2071.11), 12(Sif-1, 2071.13) and 10(Sif-1, 2071.08), and flint samples 9(Sif-1, 2070.94) and 13(Sif-1, 2079.34).

Figure 2: Atomic Force Microscopy images of: (a) sample 12(Sif-1, 2071.13), residue from chalk sample,deposited on highly oriented pyrolytic graphite (HOPG); (b) sample 13(Sif-1, 2079.34), flint. Raw sample. Samples have been imaged at room conditions in non-contact mode.

Figure 3: X-ray diffraction patterns, using 5% Si as an internal standard andCoKα-radiation; (a): sample 12(Sif-1,2071.13)residuefrom chalk sample, region 20 – 90 °2θ; (b): sample 13(Sif-1, 2079.34), flint; region 20 – 90 °2θ; (c): Quartz standard, Merck, region 20 – 90 °2θ; (d): Region of samples 12(Sif-1, 2071.13) residue from chalk sample, 13(Sif-1, 2079.34), flint and quartz standard, Merck recorded in 80 – 82 °2θ interval.

Figure 4: ^{27}Al MAS NMR spectra (14.1 T) of: (a) sample 7(Sif-1, 2065.0), flint; (b) sample 10(Sif-1, 2071.08), residue; (c) sample 17(Nana-1, 2135.8), flint. The spectra used a spinning speed of ν_R = 13.0 kHz, a short excitation pulse (0.5 μs), and a relaxation delay of 2 s.The asterisks indicate spinning sidebands.

Figure 5: ^{29}Si MAS NMR spectra of the threenano-quartzsamples (a – c) and commercial quartz (d) acquired at 9.4 T employing a spinning speed of ν_R = 6.0 kHz, a 45^o excitation pulse, and a relaxation delay of 300s. (a) sample7(Sif-1, 2065.0), flint; (b) sample 10(Sif-1, 2071.08), chalk; and (c) sample 17(Nana-1, 2135.8), flint.

Figure 6: ^{29}Si{^{1}H} CP/MAS NMR spectra (9.4 T) of the three samples (a – c) obtained with a spinning frequency of ν_R = 4.0 kHz, a 4-s relaxation delay and CP contact times

967 of τ_{CP}= 2.0 ms(left), 4.0 ms (middle), and 8.0 ms (right). (a) sample7(Sif-1, 2065.0),
968 flint; (b) sample 10(Sif-1, 2071.08), chalk; and (c) sample 17(Nana-1, 2135.8), flint.
969 Figure 7: Platelets of the aggregated $[4H]_{Si}$ defects parallel to the $(0\bar{1}010)$ plane (modified from
970 Lin et al., 1993).
971 Figure 8: Idealized structural fragments of a quartz structure in which (a) a SiO_4 tetrahedron is
972 replaced by a vacant tetrahedron coordinated by 4OH groups; and (b) tetrahedral Si^{4+}
973 is replaced by Al^{3+} and excess of negative charge is compensated by OH^- group
974 coordinated one of the four Si^{4+}tetrahedra nearest to the Al^{3+} tetrahedron. Three
975 potentially possible positions for OH^- are shown by double circles.
976 Figure 9: Infrared spectra of single pieces of specimens. Random orientation.
977 Figure 10:Relationship between the maxima of the absorption bands at 3588 and 3613cm^{-1}.
978 Figure 11: Differential thermal analysis (ΔT) with infrared determination of evolved H_2O; (a)
979 sample 12 (Sif-1, 2071.13) residue from chalk sample; (b) sample 13 (Sif-1, 2079.34),
980 flint.
981 Figure 12: Oxygen isotope composition vs. depth of sample.
982 Figure 13: Relationship between the contents of $mol^{IV}Al$ and mol(K+Na).
983 Figure 14: The idealized configuration of the hydrogarnet defects forming an OH surface parallel to
984 the (0001) plane of the quartz structure. O atoms are white circles, positions of Si
985 atoms and OH hydroxyls are marked in the figure.
986 Figure 15: Relationship between the *a* and *c* unit cell parameters of the studied samples. The almost
987 horizontal thin grey line joins positions of the samples having identical or very similar
988 values of the *a* parameter.
989 Figure 16: Relationships between the amounts of OH_y and the unit cell *a* (a) and *c* (b) parameters.

This is a preprint, the final version is subject to change, of the American Mineralogist (MSA)
Cite as Authors (Year) Title. American Mineralogist, in press.
(DOI will not work until issue is live.) DOI: http://dx.doi.org/10.2138/am-2017-5992

990 Table 1.XRD parameters for the unit cells.
991

No	Sample			Depth	*a*(Å)	*c*(Å)	*c/a*	V=*a***a***c*	*L*, nm h00	mks h00	*L*, nm h0h	mks H0h
1	Quartz	Merk<63nm	Standard 2012		4.9144	5.4055	1.0999	113.056	122(10)	0.0005	127(10)	0.0006
2	Rigs-1	White Quartz	R91675	2794.3	4.9164	5.407	1.0998	113.179	57(5)	0.001	92(5)	0.0017
3	Rigs-1	Flint	R9274 f1	2826.84	4.9169	5.4047	1.0992	113.158	50(5)	0.0016	73(5)	0.0019
4	Sif-1	Chalk (7%quartz)	6729r	2051.17	4.9182	5.4089	1.0998	113.303	72(5)	0.0009	84(5)	0.0011
5	Sif-1	Flint	6750f +23pt2	2057.63	4.9176	5.4076	1.0996	113.244	58(5)	0.0011	75(5)	0.0016
6	Sif-1	Chalk (40%quartz)	6750k	2057.65	4.918	5.4082	1.0997	113.278	63(5)	0.0011	75(5)	0.0013
7	Sif-1	Flint Lauer	Sif6774 stk9	2065.0	4.9171	5.4071	1.0997	113.214	53(5)	0.0015	81(5)	0.002
8	Sif-1	Flint Lauer	Sif67792	2066.3	4.9171	5.4058	1.0994	120.980	53(5)	0.0018	73(5)	0.0019
9	Sif-1	Flint	6793’2”x3	2070.94	4.9177	5.4074	1.0996	113.263	58(5)	0.0015	81(5)	0.0017
10	Sif-1	Chalk (29%quartz)	Sif 6793 stk1	2071.08	4.9195	5.4097	1.0997	113.377	56(5)	0.0015	68(5)	0.0017
11	Sif-1	Chalk (66%quartz)	Sif 6793 stk2	2071.11	4.9166	5.4072	1.0998	113.193	59(5)	0.0011	74(5)	0.0012
12	Sif-1	Chalk (24%quartz)	Sif 6793 stk3	2071.13	4.9186	5.4096	1.0998	113.335	56(5)	0.0014	67(5)	0.0015
13	Sif-1	Flint	6820’4”+53	2079.34	4.917	5.4063	1.0995	113.190	60(5)	0.0012	84(5)	0.0017
14	Sif-1	Flint	Sif 6851 a	2088.3	4.9172	5.4068	1.0996	113.212	70(5)	0.0011	88(5)	0.0012
15	Nana-1	Flint	6974'10"	2125.93	4.917	5.4067	1.0996	113.200	64(5)	0.0012	82(5)	0.0015
16	Nana-1	Flint	6990_	2130.55	4.9171	5.4066	1.0996	113.204	57(5)	0.0014	80(5)	0.0018
17	Nana-1	Flint	7007‘6”	2135.8	4.9171	5.4068	1.0996	113.207	47(5)	0.0016	56(5)	0.0016
18	M-10	Flint	6442 k4d4	1963.52	4.9164	5.4059	1.0996	113.154	57(5)	0.0014	80(5)	0.0018
19	E-5	Flint	6820 stkaIR	2078.74	4.9174	5.4069	1.1000	113.221	59(5)	0.0012	83(5)	0.0018

992 Errors: *a* and *c*: 0.0004 Å; mks: 0.0003Å
993

994

This is a preprint, the final version is subject to change, of the American Mineralogist (MSA)
Cite as Authors (Year) Title. American Mineralogist, in press.
(DOI will not work until issue is live.) DOI: http://dx.doi.org/10.2138/am-2017-5992

995 Table 2.Fractions of Al, K and Na determined by atomic absorption spectrometry (AAS), and relative ^{IV}Al and ^{VI}Al distribution determined
996 by ^{27}Al MAS NMR
997

Well	Sample no	Depth m	Depth '	Sample	AAS % Al_2O_3	AAS % K_2O	AAS % Na_2O	NMR ^{IV}Al %Al_2O_3	NMR ^{VI}Al %Al_2O_3
Rigs-1	2	2794.3	9167.5	Quartz layer	0.15(0.01)	0.013(0.002)	0.054 (0.008)	0.12	0.03
Rigs-1	3	2826.84	9274.41	flint	0.18(0.01)	0	0.043 (0.006)	0.16	0.02
Sif-1	5	2057.63	6750+23pt2	flint	0.14(0.01)	0.150 (0.023)	0.130 (0.013)	0.13	0.01
Sif-1	7	2065.0	6774'6"stk9	flint	0.27(0.01)	0.083(0.002)	0.075 (0.008)	0.22	0.05
Sif-1	8	2066.3	6779'4"	flint	0.19(0.01)	0.098(0.010)	0.076 (0.008)	0.15	0.04
Sif-1	9	2070.94	6793'2"x3	flint	0.33(0.02)	0.038(0.006)	0.094 (0.009)	0.29	0.04
Sif-1	10	2071.08	6793'2"stk1	residue, chalk	0.73(0.04)	0.220 (0.022)	0.600 (0.060)	0.61	0.12
Sif-1	11	2071.11	6793'2"stk2	residue, chalk	0.21(0.01)	0.005(0.001)	0.053 (0.008)	0.18	0.03
Sif-1	12	2071.13	6793'2"stk3	residue, chalk	0.39(0.02)	0.085(0.009)	0.066 (0.007)	0.24	0.15
Sif-1	13	2079.34	6820'4"+53	flint	0.34(0.02)	0.058(0.006)	0.142 (0.014)	0.28	0.06
Sif-1	14	2088.3	6851'6"	flint	0.21(0.01)	0.013(0.002)	0.050 (0.008)	0.15	0.06
Nana-1	17	2135.8	7007'6"	flint	0.11(0.01)	0.033(0.005)	0.086 (0.009)	0.09	0.02
M-10	18	1963.52	6442'k3b4	flint	0.32(0.02)	0	0.113 (0.011)	0.27	0.05
E-5	19	2078.74	6820'1"stkaIR	flint(IR)	0.38(0.02)	0	0.016 (0.002)	0.31	0.07

998
999

This is a preprint, the final version is subject to change, of the American Mineralogist (MSA)
Cite as Authors (Year) Title. American Mineralogist, in press.
(DOI will not work until issue is live.) DOI: http://dx.doi.org/10.2138/am-2017-5992

1000 Table 3. Differential thermal and evolved water analysis (DTA-EWA), 200-800°C

Well	No	Depth, m	Depth	Sample	Peak T(°C)	% H_2O	Peak T(°C)	% H_2O
Rigs-1	2	2794.3	9167.5	Quartzlayer			618	1.2
Rigs-1	3	2826.84	9274.41	flint	379	0.13	603	0.17
Sif-1	5	2057.63	6750+23pt2	flint			560	1.1
Sif-1	7	2065.0	6774’6”stk9	flint			572	1.04
Sif-1	8	2066.3	6779’4”	flint			565, 627	0.77
Sif-1	9	2070.94	6793’2”x3	flint			565	0.73
Sif-1	10	2071.08	6793’2”stk1	residue, chalk			599,697	1.9
Sif-1	11	2071.11	6793’2”stk2	residue, chalk			605, 710	1.05
Sif-1	12	2071.13	6793’2”stk3	residue, chalk			569, 650	2.1
Sif-1	13	2079.34	6820’4”+53	flint			556 (715)*	0.81
Sif-1	14	2088.3	6851’6”	flint			591	1.3
Nana-1	17	2135.8	7007’6”	flint	355	0.2	533	1.7
M-10	18	1963.52	6442’k3b4	flint			597 (760)*	0.87
E-5	19	2078.74	6820’1”stkaIR	flint(IR)			592	0.87

1001 * small shoulder; errors: % H_2O – 10%

1002

This is a preprint, the final version is subject to change, of the American Mineralogist (MSA)
Cite as Authors (Year) Title. American Mineralogist, in press.
(DOI will not work until issue is live.) DOI: http://dx.doi.org/10.2138/am-2017-5992

1003 Table 4.Chemical formulaefor the quartz samples from ^{27}Al NMR, Atomic Absorption Spectrometry and thermal analysis (EGA)

1004

Well	Sample	Depth m	Mol K	Mol Na	Mol^{IV}Al	Mol^{VI}Al	Mol Al	Mol Si	Vacancy tetrahedral	Mol O	Mol OH_y	Mol OH_m	Mol $OH(^{VI}Al)$*
Rigs-1	2 quartz	2794.3	0.0001	0.0009	0.0012	0.0003	0.0015	0.982	0.0164	1.934	0.0656	0.0002	0.0009
Rigs-1	3 flint	2826.84	0.0000	0.0007	0.0016	0.0002	0.0018	0.995	0.0038	1.985	0.0152	0.0009	0.0006
Sif-1	5 flint	2057.63	0.0016	0.0021	0.0013	0.0001	0.0014	0.984	0.0146	1.942	0.0584	0.0024	0.0003
Sif-1	7 flint	2065.0	0.0009	0.0012	0.0022	0.0005	0.0026	0.984	0.0140	1.944	0.0562	0.0001	0.0015
Sif-1	8 flint	2066.3	0.0010	0.0012	0.0015	0.0004	0.0019	0.988	0.0102	1.959	0.0408	0.0008	0.0012
Sif-1	9 flint	2070.94	0.0004	0.0015	0.0028	0.0004	0.0032	0.988	0.0096	1.962	0.0384	0.0009	0.0012
Sif-1	10 residue	2071.08	0.0023	0.0097	0.0060	0.0012	0.0072	0.969	0.0240	1.904	0.0959	0.0060	0.0035
Sif-1	11 residue	2071.11	0.0001	0.0009	0.0018	0.0003	0.0021	0.984	0.0141	1.943	0.0565	0.0009	0.0009
Sif-1	12 residue	2071.13	0.0009	0.0011	0.0024	0.0015	0.0038	0.970	0.0279	1.888	0.1118	0.0004	0.0044
Sif-1	13 flint	2079.34	0.0006	0.0023	0.0027	0.0006	0.0033	0.986	0.0108	1.957	0.0430	0.0002	0.0018
Sif-1	14 flint	2088.3	0.0001	0.0008	0.0015	0.0006	0.0021	0.981	0.0175	1.930	0.0699	0.0005	0.0018
Nana-1	17 flint	2135.8	0.0004	0.0014	0.0009	0.0002	0.0011	0.973	0.0260	1.896	0.1040	0.0009	0.0006
M-10	18 flint	1963.52	0.0000	0.0018	0.0026	0.0005	0.0031	0.986	0.0115	1.954	0.0460	0.0008	0.0015
E-5	19 flint	2078.74	0.0000	0.0003	0.0030	0.0007	0.0037	0.987	0.0109	1.957	0.0435	0.0028	0.0021

1005 #contains probably layer silicates; *OH assumed to be bonded to ^{VI}Al

1006

1007 Table5. Oxygen isotope data
1008

No	Sample	Depth, m	$\delta^{18}O$ (‰V-SMOV)
2	Rigs-1, 9167.5'	2794.3	24.9
3	Rigs-1, 9274.41'	2826.84	24.9
5	Sif-1, 6750 pr.2	2057.63	28.5
7	Sif-1, 6774' stk9	2065	28.3
8	Sif-1, 6779'4"	2066.3	28.4
10	Sif-1, 6793' stk1	2071.08	26.4
11	Sif-1, 6793' stk2	2071.11	26.8
12	Sif-1, 6793' stk3	2071.13	27.6
13	Sif-1, 6820	2079.34	27.9
14	Sif-1, 6851'a	2088.3	26.5
17	Nana-1, 7007'	2135.8	28.9
18	M-10, 6442	1963.52	29.4
19	E-5, 6820	2078.74	28.8

1009

1010

This is a preprint, the final version is subject to change, of the American Mineralogist (MSA)
Cite as Authors (Year) Title. American Mineralogist, in press.
(DOI will not work until issue is live.) DOI: http://dx.doi.org/10.2138/am-2017-5992

1011 Table 6. Ranges for the *a*- and *c*- unit cell parameters compared with literature data.

	Natural samples		Synthetic samples	
	a-unit cell parameter	*c*-unit cell parameter	*a*-unit cell parameter	*c*-unit cell parameter
Present investigation	4.9164-4.9195 Å	5.4047-5.4097 Å		
Anafas'eva et al. (1960)	4.9121-4.9137 Å	5.4038-5.4051 Å		
Cohen and Sumner (1958)	4.9131-4.9138 Å	5.4047-5.4052 Å	4.9132-4.9139 Å	5.4049-5.4052 Å
Hurst and Storch (1982)	4.9133-4.9140 Å	5.4044-5.4054 Å		
Brice (1980)	4.9126-4.9149 Å		4.9133-4.9145 Å	

This is a preprint, the final version is subject to change, of the American Mineralogist (MSA)
Cite as Authors (Year) Title. American Mineralogist, in press.
(DOI will not work until issue is live.) DOI: http://dx.doi.org/10.2138/am-2017-5992

012

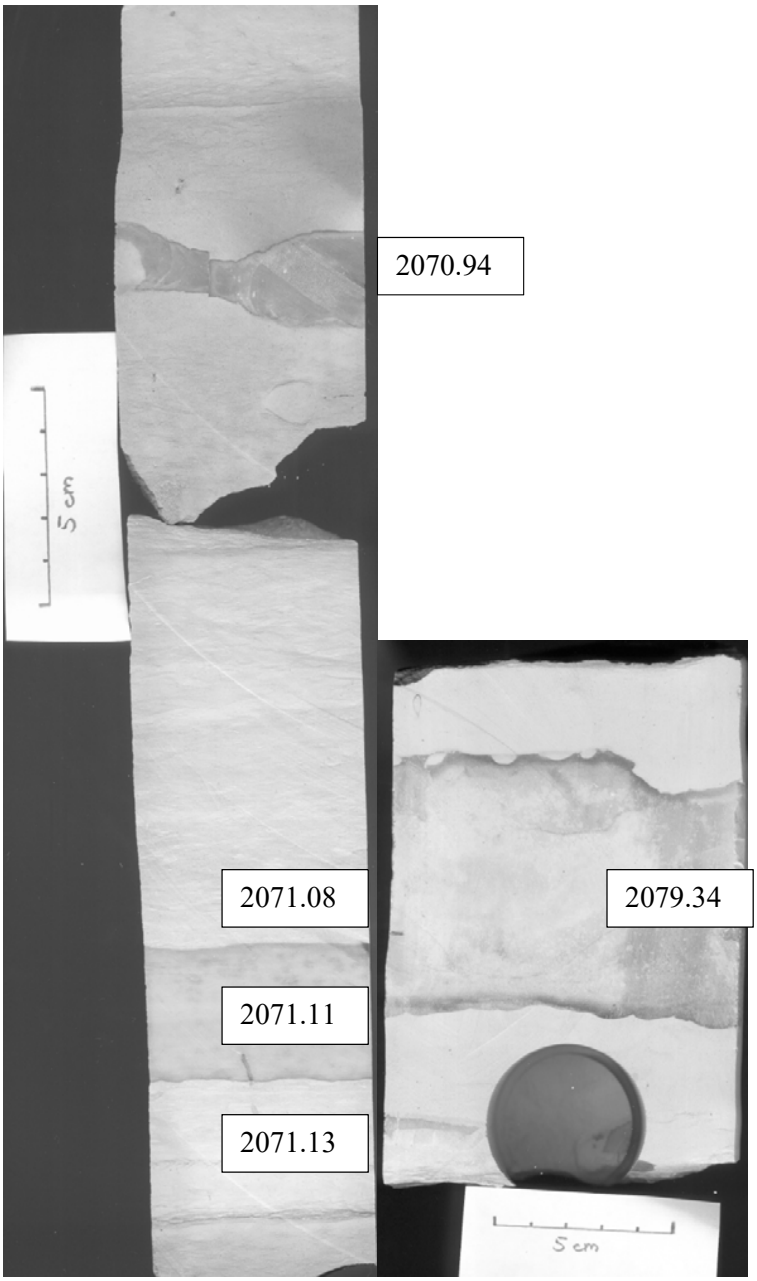

013

014

015 Figure 1.

016

This is a preprint, the final version is subject to change, of the American Mineralogist (MSA)
Cite as Authors (Year) Title. American Mineralogist, in press.
(DOI will not work until issue is live.) DOI: http://dx.doi.org/10.2138/am-2017-5992

017

018

019

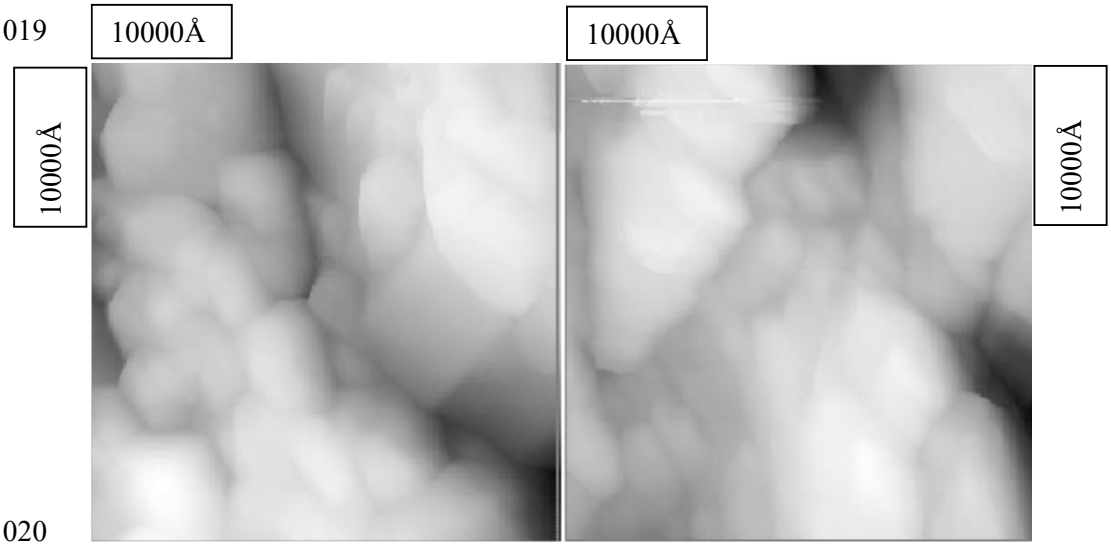

020

021

022 Figure 2a. Figure 2b.

023

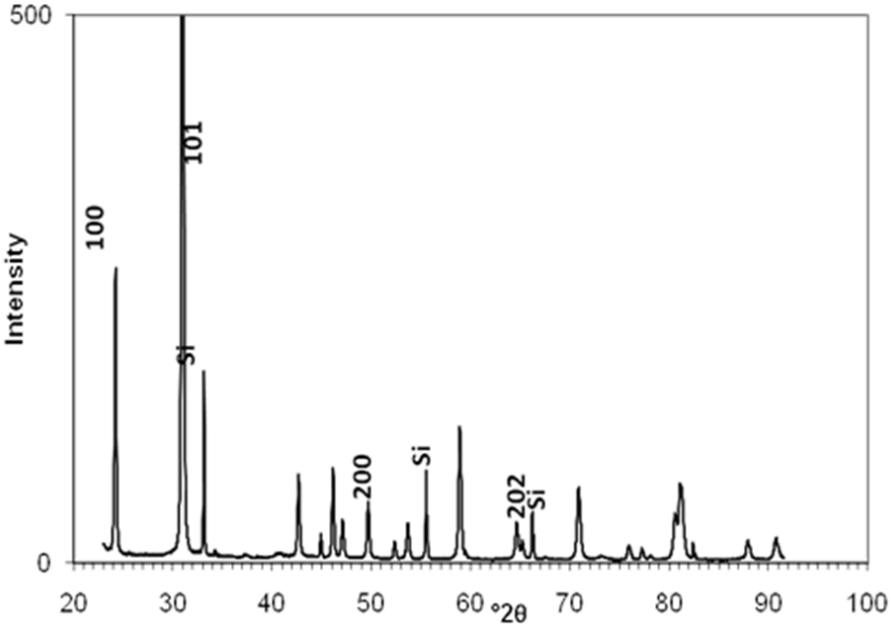

Figure 3a.

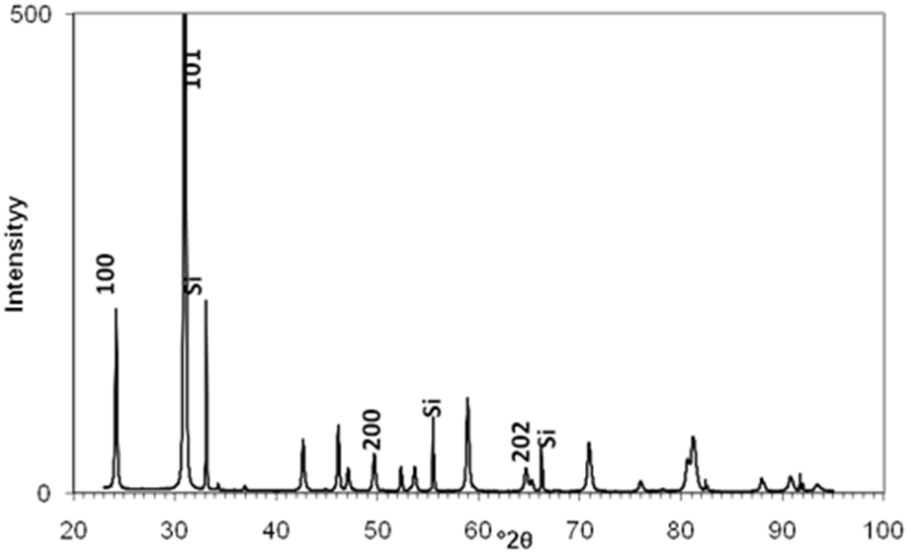

Figure 3b.

034

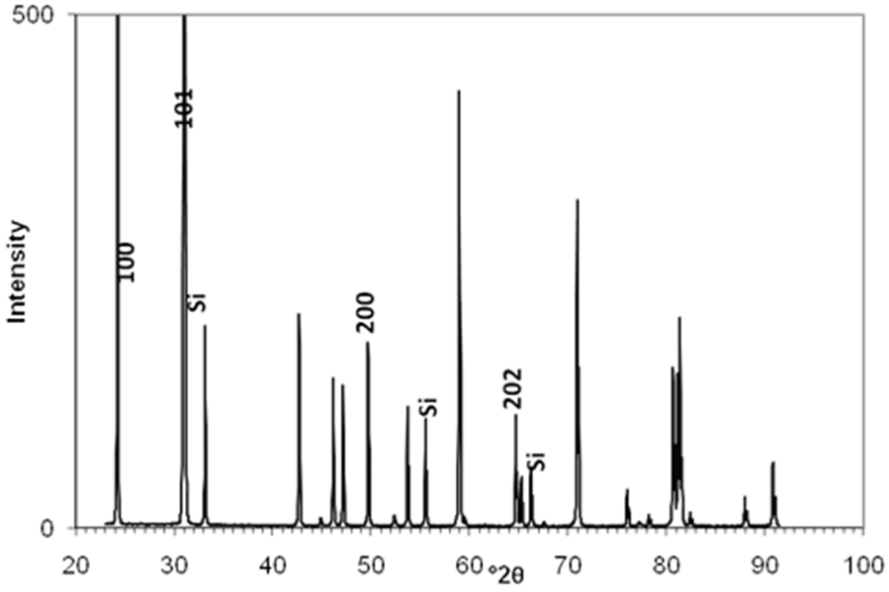

035
036
037 Figure 3c.
038
039

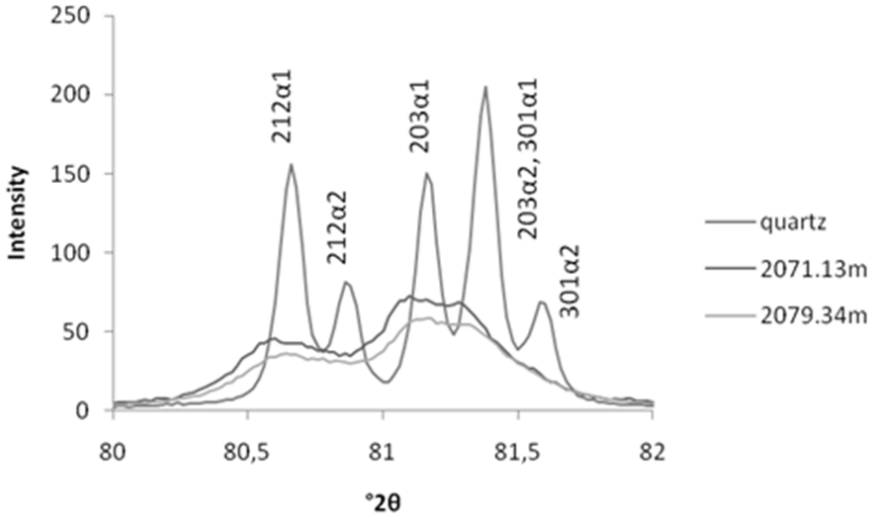

040
041
042 Figure 3d.
043

This is a preprint, the final version is subject to change, of the American Mineralogist (MSA)
Cite as Authors (Year) Title. American Mineralogist, in press.
(DOI will not work until issue is live.) DOI: http://dx.doi.org/10.2138/am-2017-5992

044

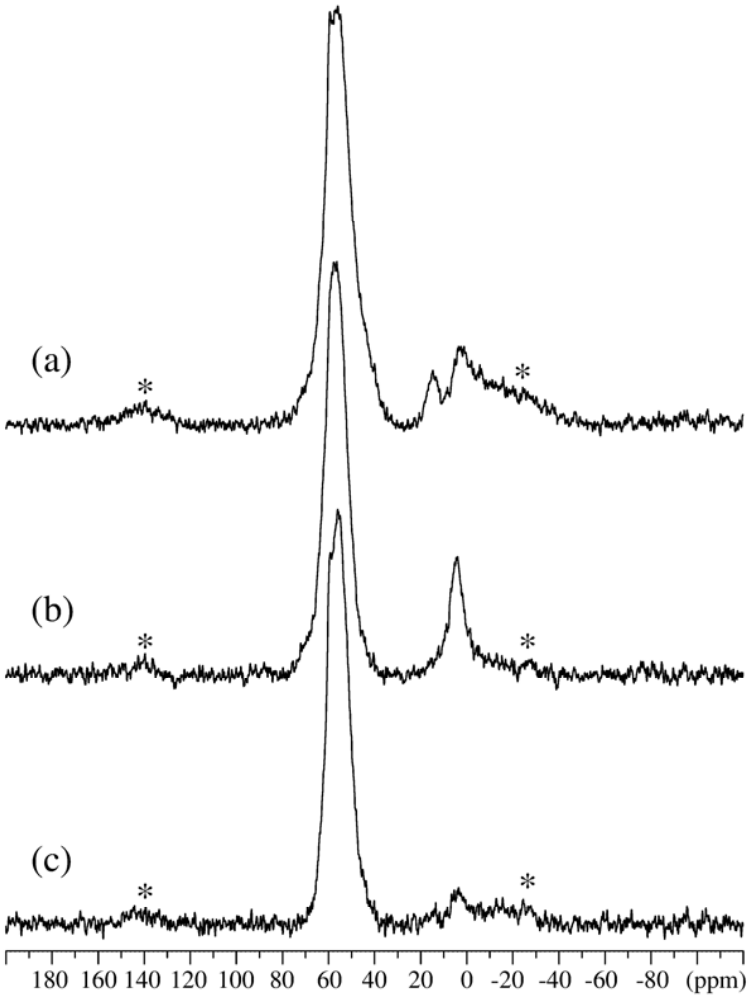

045

046 Figure 4.

047

This is a preprint, the final version is subject to change, of the American Mineralogist (MSA)
Cite as Authors (Year) Title. American Mineralogist, in press.
(DOI will not work until issue is live.) DOI: http://dx.doi.org/10.2138/am-2017-5992

048

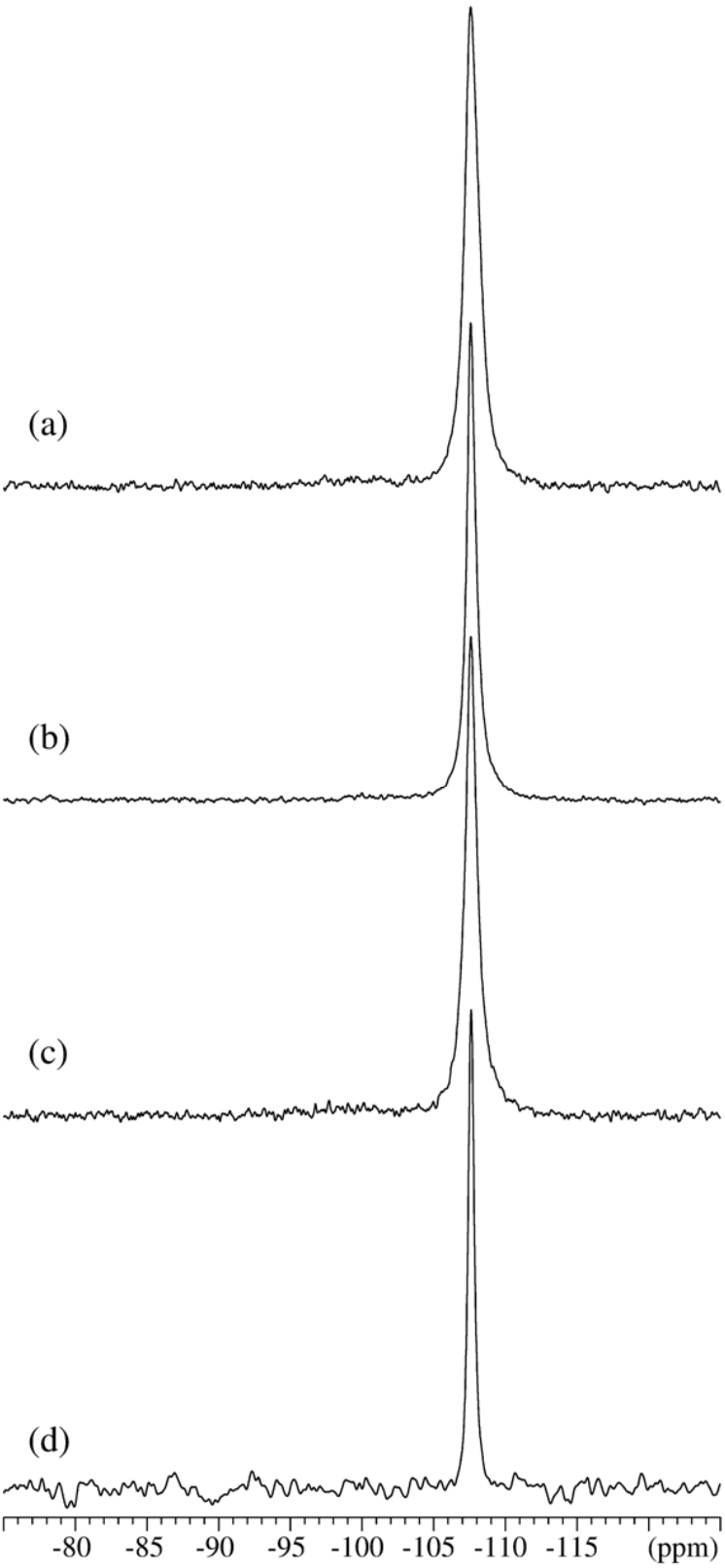

049
050 Figure 5.
051

This is a preprint, the final version is subject to change, of the American Mineralogist (MSA)
Cite as Authors (Year) Title. American Mineralogist, in press.
(DOI will not work until issue is live.) DOI: http://dx.doi.org/10.2138/am-2017-5992

052

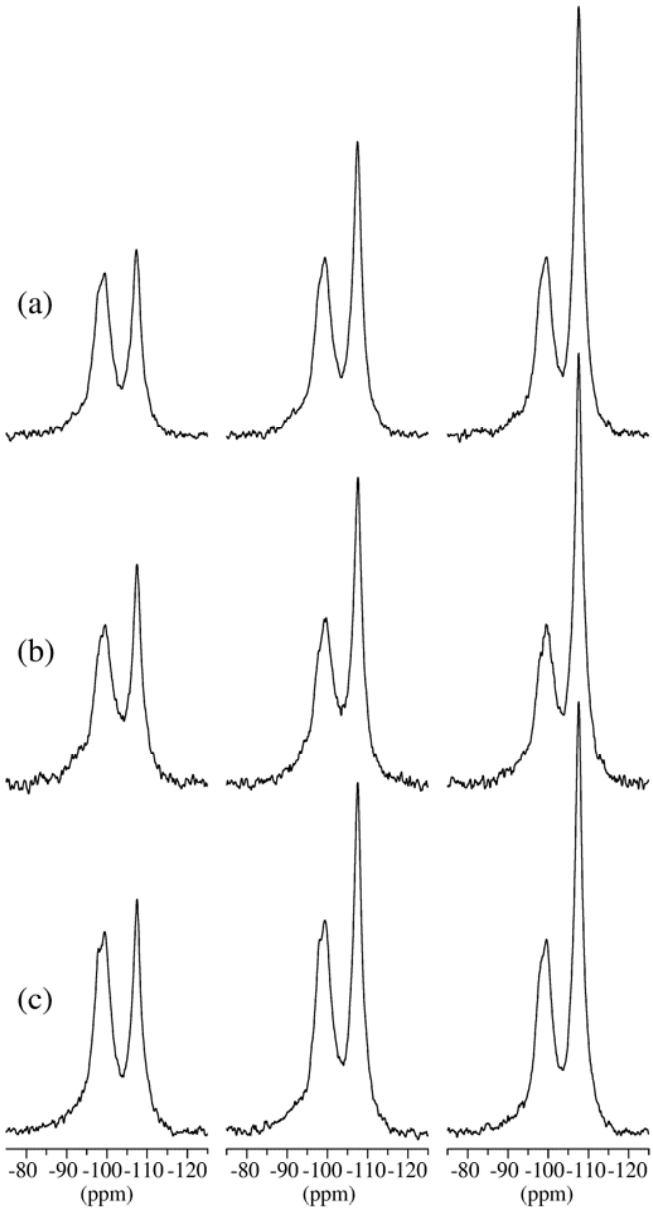

053

054

055 Figure 6.

056

This is a preprint, the final version is subject to change, of the American Mineralogist (MSA)
Cite as Authors (Year) Title. American Mineralogist, in press.
(DOI will not work until issue is live.) DOI: http://dx.doi.org/10.2138/am-2017-5992

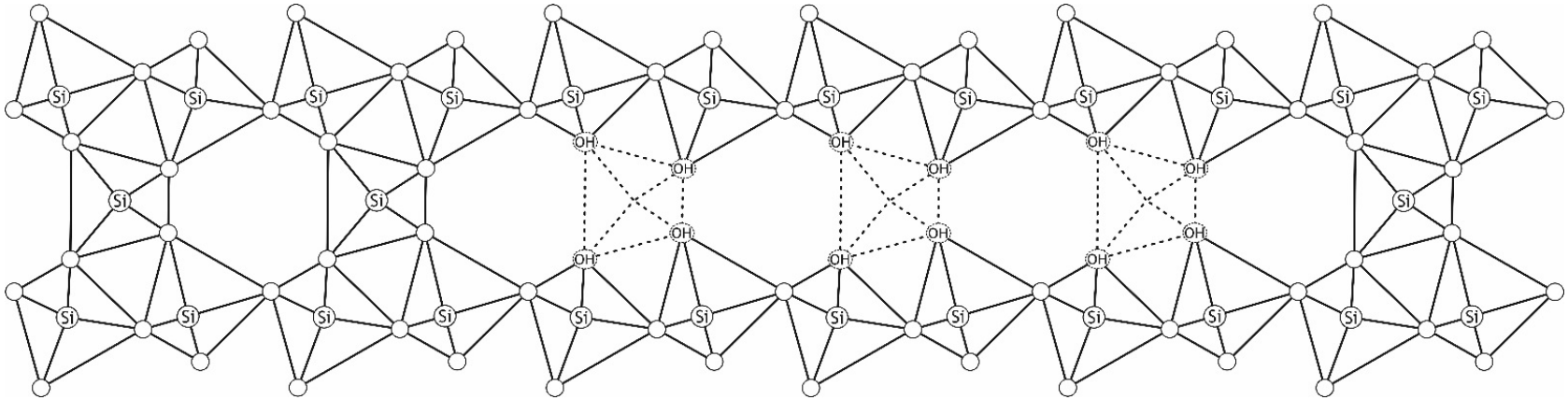

Figure 7.

a) b)

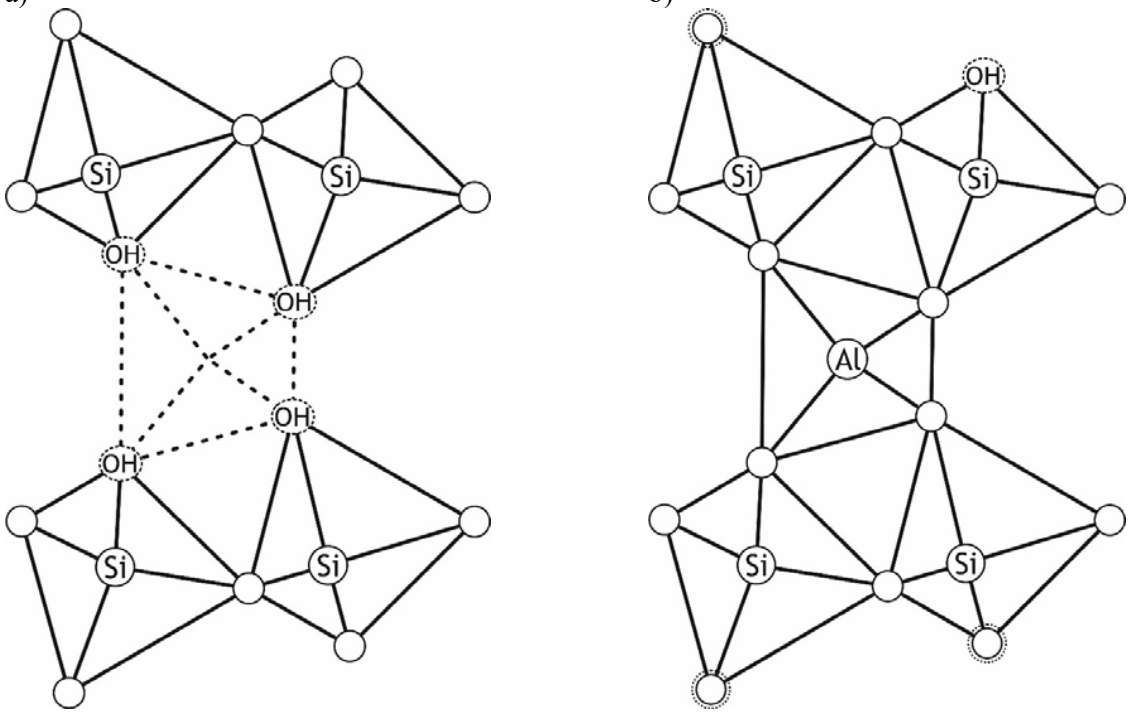

Figure 8.

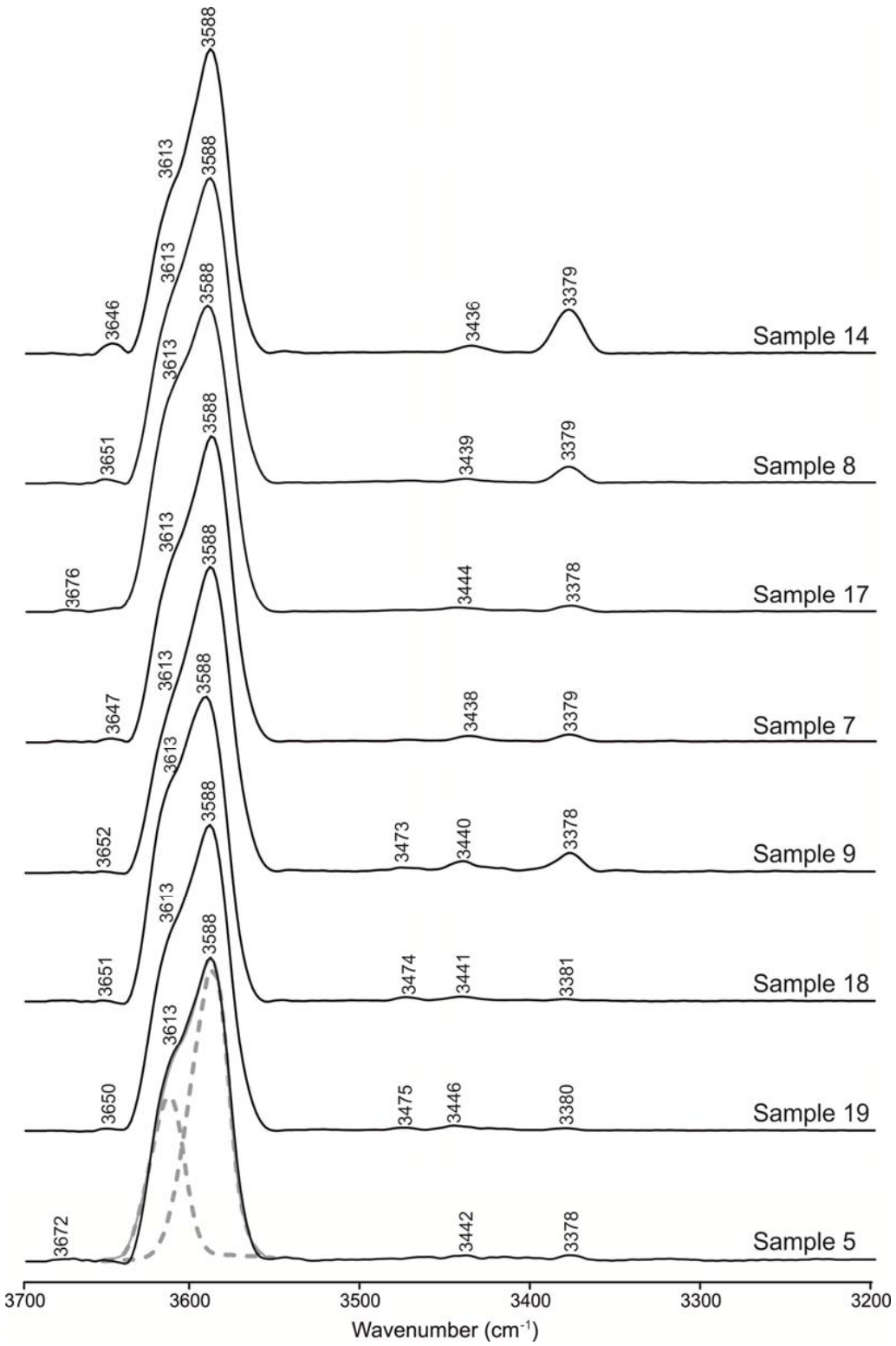
3588
3613
3646
3436
3379
Sample 14
3651
3439
Sample 8
3676
3444
3378
Sample 17
3647
3438
Sample 7
3652
3473
3440
Sample 9
3474
3441
3381
Sample 18
3650
3475
3446
3380
Sample 19
3672
3442
Sample 5
3700
3600
3500
3400
3300
3200
Wavenumber (cm-1)

Figure 9.

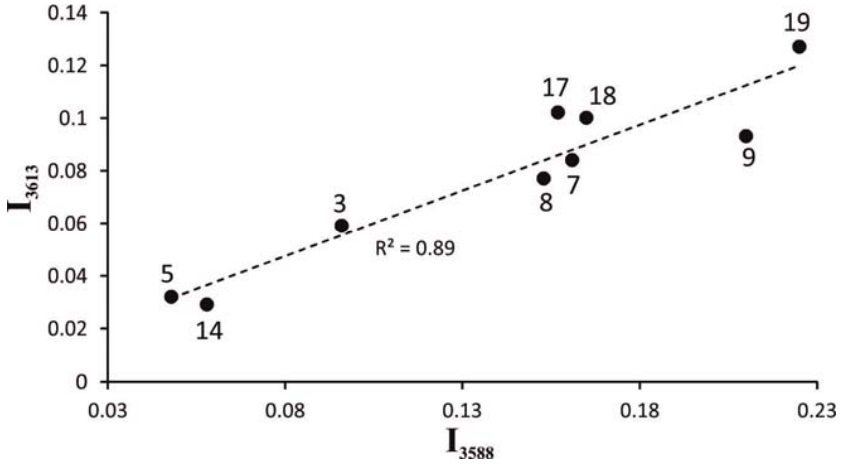
0.14
0.12
0.1
0.08
0.06
0.04
0.02
0
0.03
0.08
0.13
0.18
0.23
I3613
I3588
R² = 0.89
19
17
18
9
7
8
3
5
14

Figure 10

a)

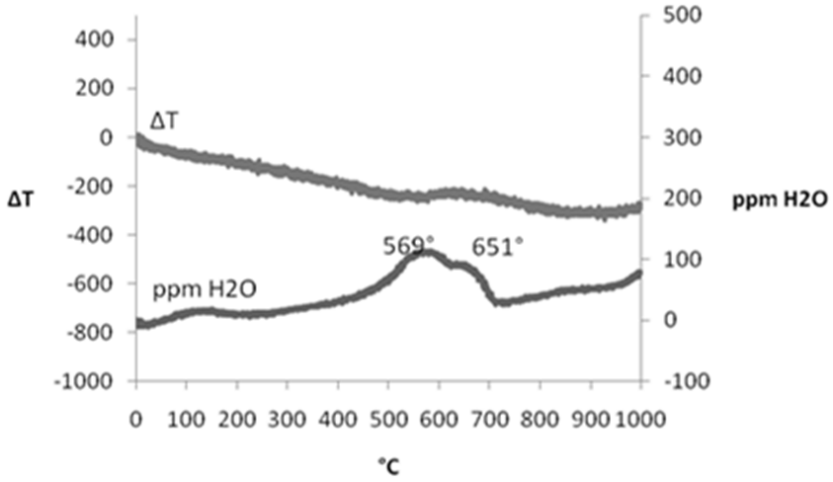
ΔT
ppm H2O
569°
651°
400
200
0
-200
-400
-600
-800
-1000
500
400
300
200
100
0
-100
0 100 200 300 400 500 600 700 800 900 1000
°C

b)

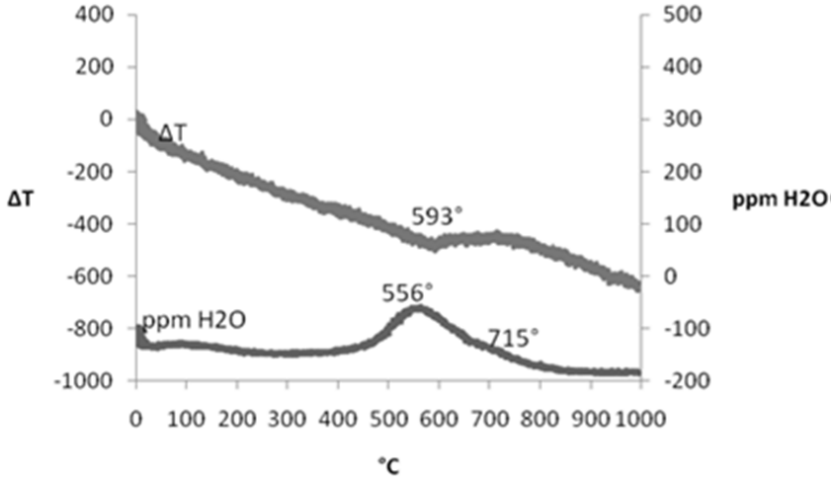
ΔT
ppm H2O
593°
556°
715°
400
200
0
-200
-400
-600
-800
-1000
500
400
300
200
100
0
-100
-200
0 100 200 300 400 500 600 700 800 900 1000
°C

Figure 11.

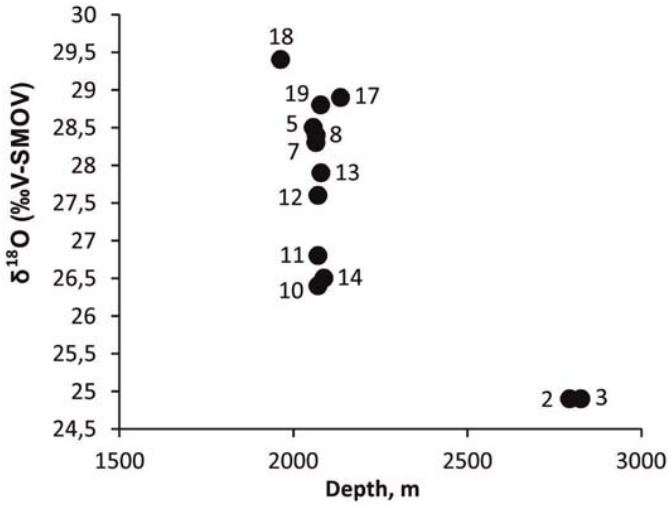

1080

1081

1082 Figure 12.

1083

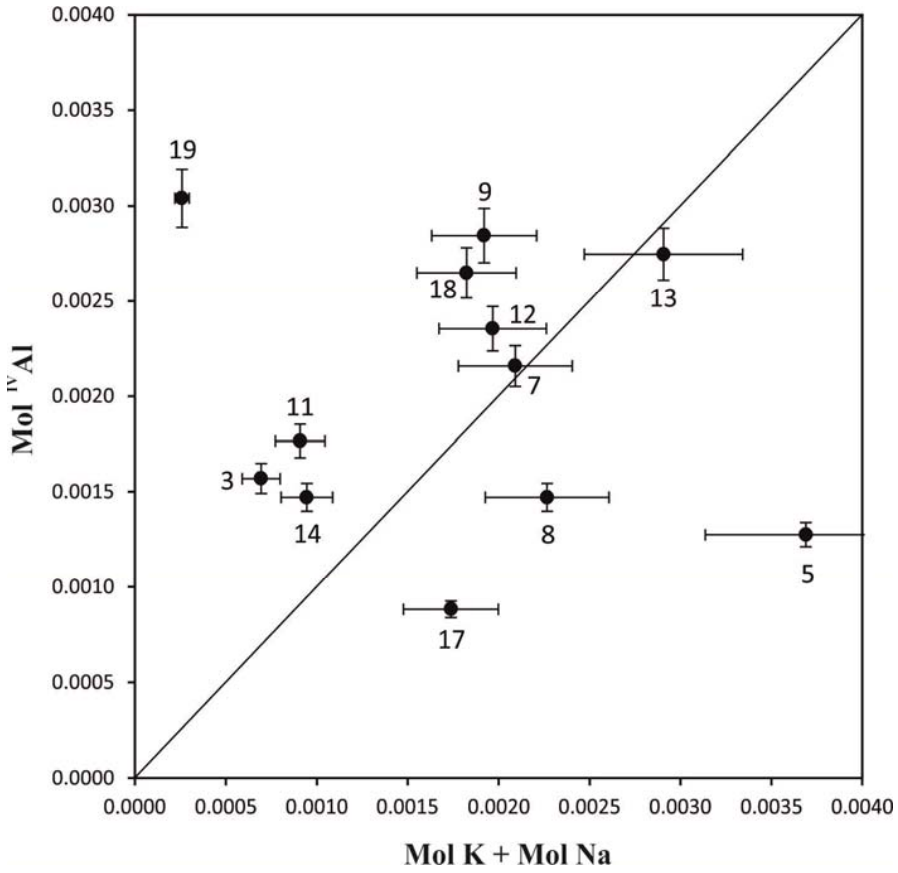
0.0040
0.0035
0.0030
0.0025
0.0020
0.0015
0.0010
0.0005
0.0000
Mol IVAl
0.0000
0.0005
0.0010
0.0015
0.0020
0.0025
0.0030
0.0035
0.0040
Mol K + Mol Na
19
9
18
12
13
7
11
3
14
8
5
17

Figure 13.

This is a preprint, the final version is subject to change, of the American Mineralogist (MSA)
Cite as Authors (Year) Title. American Mineralogist, in press.
(DOI will not work until issue is live.) DOI: http://dx.doi.org/10.2138/am-2017-5992

1088

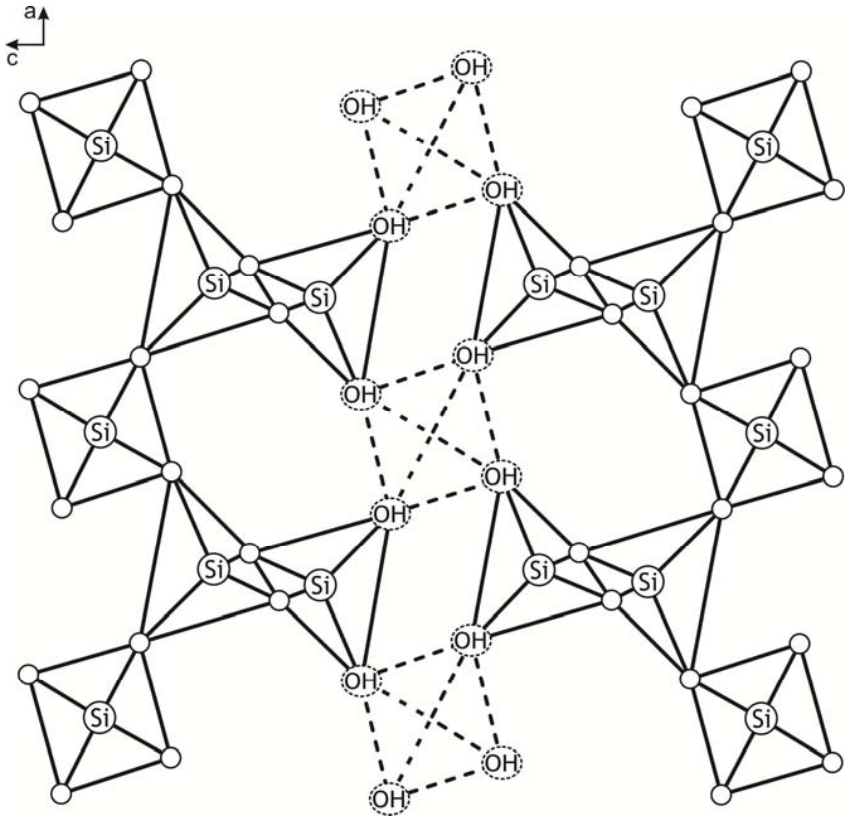

1089
1090
1091 Figure 14.
1092

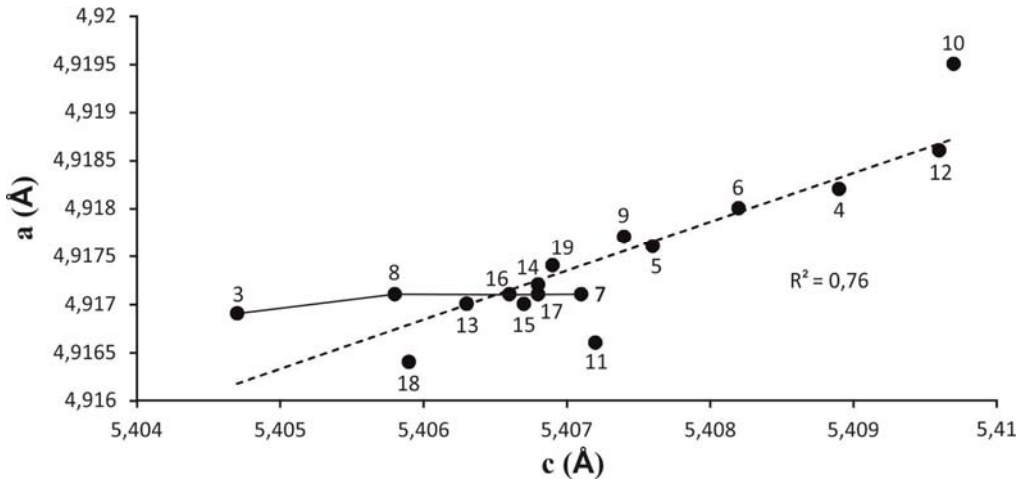
4,92
4,9195
4,919
4,9185
4,918
4,9175
4,917
4,9165
4,916
a (Å)
5,404
5,405
5,406
5,407
5,408
5,409
5,41
c (Å)
R² = 0,76
10
12
6
4
9
5
19
14
16
8
3
7
17
13
15
18
11

Figure 15.

a)

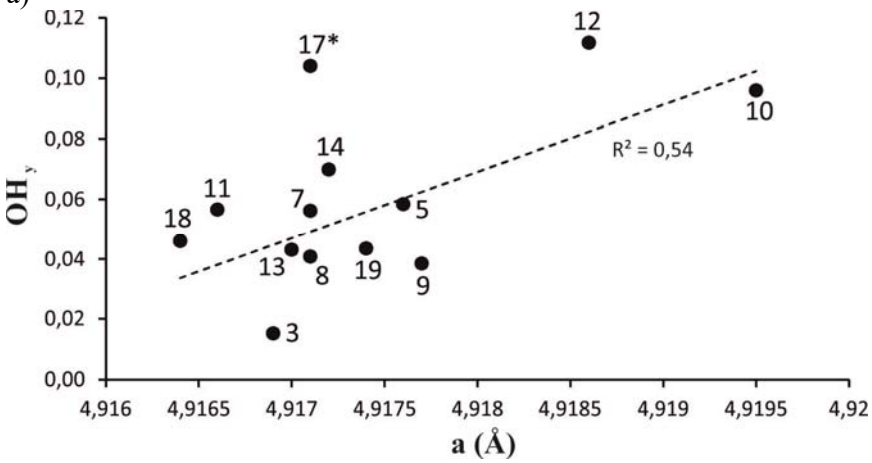
0,12
0,10
0,08
0,06
0,04
0,02
0,00
OH$_y$
4,916
4,9165
4,917
4,9175
4,918
4,9185
4,919
4,9195
4,92
a (Å)
R² = 0,54
17*
12
10
14
11
7
5
18
13
8
19
9
3

b)

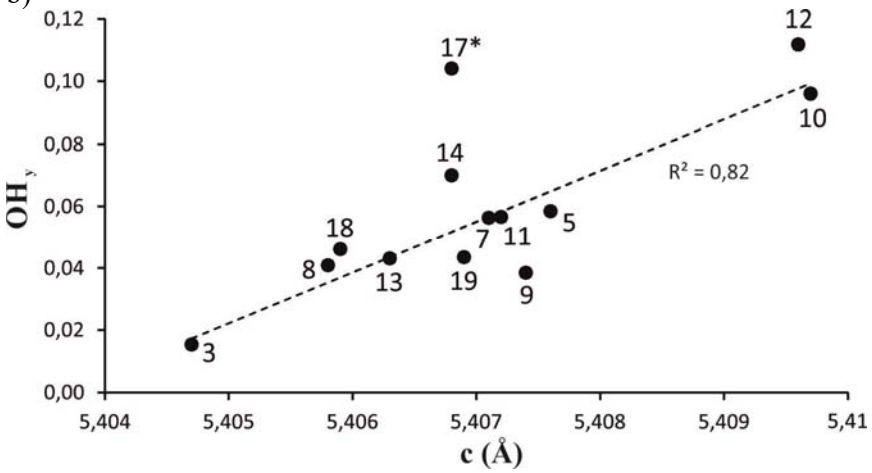
0,12
0,10
0,08
0,06
0,04
0,02
0,00
OH$_y$
5,404
5,405
5,406
5,407
5,408
5,409
5,41
c (Å)
R² = 0,82
17*
12
10
14
18
8
13
7
11
19
5
9
3

Figure 16.